CHALMERS
UNIVERSITY OF TECHNOLOGY

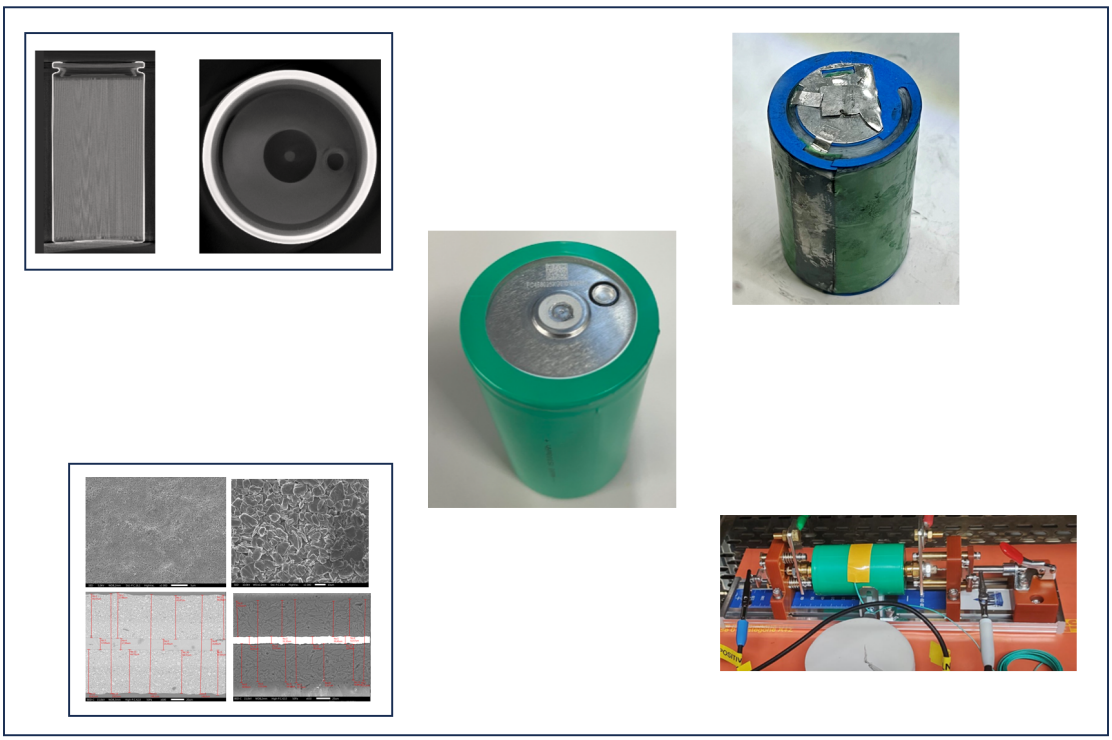

Characterisation of a 4680 Cylindrical Cell: Insights Into Cell Design and Performance

Master's thesis in Mobility Engineering (Automotive track)

PREMKRISHNAN NAIR

DEPARTMENT OF INDUSTRIAL AND MATERIALS SCIENCE
CHALMERS UNIVERSITY OF TECHNOLOGY
Gothenburg, Sweden 2024
www.chalmers.se

Master's thesis 2024

Characterization of a 4680 Cylindrical Cell: Insights Into Cell Design and Performance

PREMKRISHNAN NAIR

CHALMERS
UNIVERSITY OF TECHNOLOGY

Division of Materials and Manufacture
Department of Industrial and Materials Science
Chalmers University of Technology
Gothenburg, Sweden 2024

Characterization of a 4680 Cylindrical Cell: Insights Into Cell Design and Performance
PREMKRISHNAN NAIR

Supervisor: Andrea Boschin, Volvo Cars, Battery Cell Design
Examiner: Jinhua Sun, Department of Industrial and Materials Science

Master's Thesis 2024
Division of Materials and Manufacture
Department of Industrial and Materials Science
Chalmers University of Technology
SE-412 96 Gothenburg
Telephone +46 31 772 1000

Cover: CT Scan image of the cell, SEM image for electrodes, cell as received, jellyroll and setup for electrical testing of a BYD 4680 cell

Typeset in LaTeX
Printed by Chalmers Reproservice
Gothenburg, Sweden 2024

Characterization of a 4680 Cylindrical Cell: Insights Into Cell Design and Performance

PREMKRISHNAN NAIR
Department of Industrial and Materials Science
Chalmers University of Technology

Abstract

Li-ion batteries are expected to tackle the demands of powering the automotive industry shift toward electrification. Selecting the right components by considering attributes like performance, safety, and longevity is crucial. These batteries come in various forms: cylindrical, pouch, and prismatic, each with its own set of pros and cons in terms of manufacturing, packaging, energy and power. Recently, there has been a proposal for cylindrical cells of the 46xx series, which allows increased capacity, potentially making them more viable for battery packs. This project aims to provide insights into the design and electrical testing of a 4680 cylindrical Li-ion cell with a lithium iron phosphate (LFP) cathode. This cell chemistry has recently gained more interest within the automotive sector due to its cost and safety.

Insights into the cell design have been obtained through a thorough cell-teardown process. Unlike prismatic cells, which typically use aluminum cans, the cylindrical cell features a steel can, presenting unique challenges during the disassembly process. To address this, two methodologies for opening cylindrical cells were developed and reviewed. Additionally, the design for the cell considered within this study differs from existing tabless architectures for 4680 cylindrical cells found in literature.

The materials harvested from the cell teardown were characterized to obtain information about the cell components, such as electrodes, electrolyte, separators, tabs, etc. Furthermore, electrical testing methods such as galvanostatic charge and discharge, hybrid pulse power characterization, and electrochemical impedance spectroscopy (EIS) provided additional valuable insights into cell performance.

This study contributes to the benchmarking of 4680 cylindrical cell series, which are otherwise scarcely documented in literature.

Keywords: Cylindrical cells, cell design, teardown, electrical testing

Acknowledgements

This thesis work has been conducted within the Cell Design team at Volvo Cars, Sweden, and I am deeply grateful for the unwavering support of my supervisor, Andrea Boschin. His invaluable feedback, guidance, and encouragement have been instrumental in the success of this project.

I also extend my gratitude to Leopold Werberg, Nandeep Mysore, and Bertrand Philippe for their outstanding support throughout the thesis, particularly in deciphering cell scans and assisting in the design of teardown equipment. I am thankful for the assistance provided by Parth Dayama, Muhammad Bhatti and Felix Braun the test engineers at the Battery Laboratory, as well as Lisa Lundberg Lenell, Madeleine Stoopendahl and Anna-Karin Uveborn at the Material Center. I'm also grateful to Andreas Flood from the Strength Test Lab, cell design team and the battery testing & prep team especially Adam Wallengren and Victor Oskarsson for all the help and support I have received.

Special thanks to Jinhua Sun, my examiner at Chalmers, for his patience, invaluable feedback on the report and guidance during the thesis work.

Lastly, I am deeply grateful to my family, especially my late mother, who has always been a constant source of strength and motivation. I also extend my heartfelt thanks to my friends for their unwavering encouragement and support throughout my journey at Volvo Cars Corporation.

Premkrishnan Nair, Gothenburg, June 2024

List of Acronyms

Below is the list of acronyms that have been used throughout this thesis listed in alphabetical order:

ATR	Attenuated Total Reflectance
BES	Battery Energy Storage
CC-CV	Constant Current-Constant Voltage
DCIR	Direct Current Internal Resistance
DMC	Dimethyl Carbonate
DSC	Differential Scanning Calorimetry
EC	Equivalent Circuit
ECM	Equivalent Circuit Model
EDX	Energy Dispersive X-Ray Spectroscopy
EIS	Electrochemical Impedance Spectroscopy
EMC	Ethyl Methyl Carbonate
EVs	Electric Vehicles
FTIR	Fourier Transform Infrared Spectroscopy
GEIS	Galvanostatic Electrochemical Impedance Spectroscopy
LFP	Lithium Iron Phosphate
LIBs	Lithium-ion Batteries
NE	Negative Electrode
OCV	Open Circuit Voltage
PE	Positive Electrode
PET	Polyethylene Terephthalate
RCT	Rate Capability Test
RPT	Reference Performance Test
SEM	Scanning Electron Microscopy
SOC	State of Charge
TO	Test Object
XCT	X-ray Computed Tomography

Contents

List of Figures

List of Tables

1
Introduction

1.1 Background

Energy storage systems promising better performance, safety and affordability are becoming more and more necessary as the market for EVs expands. Lithium-ion batteries (LIBs) have become the preferred energy source in electric vehicles (EVs) due to their high energy density, low self-discharge rate, and long cycle life. Since their commercialization, different formats of Li-ion cells have been proposed, based on the application required. Mainly in the automotive industry, the most common formats used are pouch, prismatic and cylindrical cells [1]. The release of Tesla Model S and X showed that cylindrical cell formats (18650: 18 mm diameter and 65 mm height) could be used as an energy source for EVs [6]. The Tesla Model Y, presented during Battery Day, features large format cylindrical cells (4680: 46 mm diameter and 80 mm height) tabless design. This design has shown better performance by improving tab-cooling topology and increased efficiency through better mitigation of ohmic losses [7, 8].

The large-format cylindrical cells when compared to cells with smaller dimensions have increased energy per cell, which will help mitigate overall costs by using fewer cells, thereby reducing the connections required for the same energy inside a pack. Such cylindrical cells are becoming increasingly popular in the automotive industry. Companies like BMW have announced the use of cylindrical cells in their latest electric vehicle platform called "Neue Klasse" which will house cells having a 46 mm diameter coupled with two different heights [9].

To meet application requirements such as energy, power, and safety, it is essential to optimize both the design of the cell and the system. Insights into the design of these cells can be gained through teardown and analysis of the extracted components. Additionally, performance can be evaluated through electrical testing, ensuring that the battery meets the necessary specifications.

1.2 Objective

This thesis focuses on optimizing methods for characterizing the 46xx series cylindrical cells. The cell considered in this work is a BYD 4680 cylindrical cell of lithium iron phosphate (LFP) chemistry. Cell characterization encompasses material analysis and basic electrical tests. The teardown is performed in a glove box and its different components are analyzed qualitatively and quantitatively. Prior to performing a cell teardown to extract the relevant components, an X-ray computed tomography (XCT) scan was performed. Material and component analysis was performed with Scanning Electron Microscope (SEM) and Energy Dispersive X-ray

Spectroscopy (EDX) among others. Electrical characterization was conducted using various tests, including Galvanostatic Electrochemical Impedance Spectroscopy (GEIS), Reference Performance Test (RPT), and Rate Capability Tests (RCTs).

1.3 Sustainability

With an emphasis on large-format 4680 cylindrical cell characterization and benchmarking, this research closely relates to multiple Sustainable Development Goals (SDGs) [10]. In particular, by advancing research in energy storage technologies that are essential for sustainable power sources, it advances SDG 7 (Affordable and Clean Energy) [11]. Furthermore, this work contributes to SDG 9 (Industry, Innovation, and Infrastructure) [12] and SDG 13 (Climate Action) [13] with the aim to improving the performance and efficiency of electric vehicle (EV) batteries, which in turn helps to accelerate the transition to cleaner transportation systems. In addition, LFP chemistry utilizes more abundant and relatively more environmentally friendly materials, thereby reducing the environmental impact concerning battery manufacturing and disposal and contributing to SDG 12, which promotes responsible consumption and production [14]. Using comprehensive characterization and benchmarking, this study contributes to the larger objective of developing sustainable transportation solutions that lower greenhouse gas emissions and lessen the effects of climate change, thus laying the foundation for developing more reliable, long-lasting and ecologically friendly batteries.

1.4 Ethics

Ethical principles are integral to both academic and professional engineering. It is crucial to maintain confidentiality, provide proper acknowledgment, ensure objectivity and originality, and follow ethical data collection practices when presenting findings. In this report, sensitive data is partially disclosed to comply with confidentiality protocols, and all collected data adheres to ethical guidelines and regulations.

2

Theory

This section describes the working principle of a Li-ion battery and the different techniques used through this work for the electrical and material characterization of a BYD 4680 cylindrical cell such as EIS, RPT, RCTs, SEM-EDX etc.

2.1 Lithium-ion Batteries

Batteries are electrochemical devices that convert the chemical energy present in their active materials into electrical energy via an electrochemical oxidation-reduction (redox) reaction [15]. The battery is often referred to as one or more electrochemical cells connected in series or parallel circuit. A battery could be either primary or secondary. Primary batteries can only be discharged while secondary batteries are rechargeable. It consists of two electrodes separated by a separator, enabling the flow of ions while preventing direct contact between the electrodes, thereby converting chemical energy to electrical energy. An essential component of this process is the electrolyte, which facilitates the movement of ions between the electrodes. To guarantee effective ion transport while avoiding electrical short circuits, it must be ionically conductive and electronically insulating. It can be a liquid, gel, or solid. LIBs are the most popular type of rechargeable battery used nowadays. They have lithium ions serving as charge carriers moving between the electrodes, resulting in the charge or discharge of the cell. During a discharge, the ions move from the negative electrode to the positive electrode through the separator and electrons flow from the negative to the positive electrode through the external circuit. The opposite happens during charge. As a result, the negative electrode acts as an anode (where an oxidation reaction takes place) during discharge and as a cathode (where the electrochemical reaction is a reduction) during charge. The positive electrode is instead a cathode during discharge and an anode when the cell is charged. Although the International Union of Pure and Applied Chemistry (IUPAC) recommends the usage of positive electrode and negative electrode [16], in this thesis, to avoid repeating those terms too often and for the sake of readability, the discharge process is considered and the terms positive electrode and cathode, negative electrode and anode, will be used interchangeably. Some common lithium-ion battery cathodes include lithium iron phosphate (LFP), lithium nickel-manganese-cobalt (NMC), and lithium cobalt oxide (LCO), while anodes typically consist of materials such as graphite, silicon-based anodes, and lithium titanium oxide (LTO) [17].

The different cell formats used in the automotive industry are pouch, prismatic and cylindrical cells [1]. The primary distinction lies in the cell-casing design as well as the layout of the anode, cathode and separators. A hard casing enclosure composed of aluminium or steel is used for prismatic and cylindrical cells. The

cylindrical cells have jellyrolls which are winded. The pouch cells have a relatively soft aluminium packet enclosure. In prismatic cells, the jelly rolls are winded or stacked and are placed inside a cuboid enclosure box [18]. The pouch cells follow stack-like arrangement of electrodes [1, 19, 18] inside a laminated aluminum pouch enclosure. Some standard cell formats are mentioned in the figure below. The cylindrical cell structure is explained in the next section.

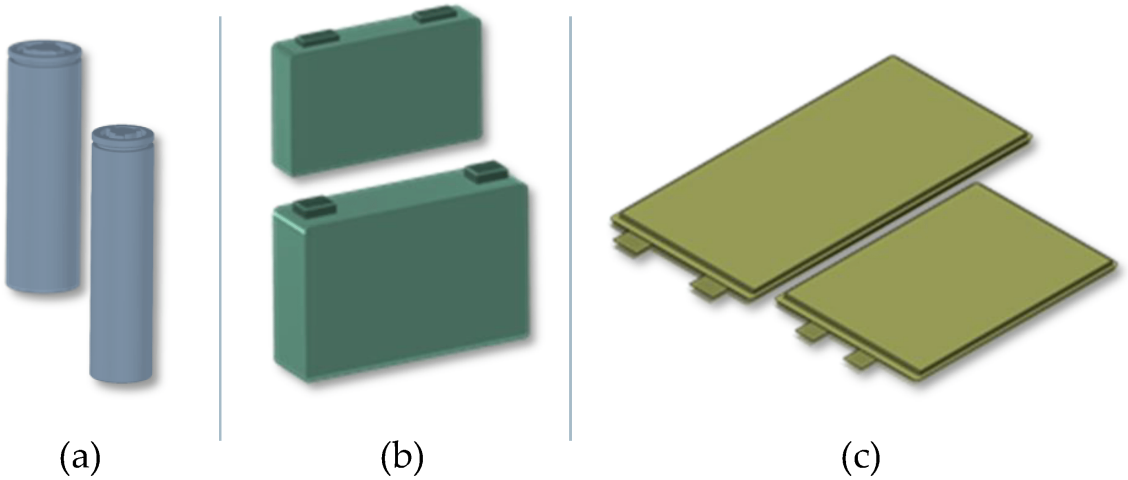

Figure 2.1: Various cell-formats: (a) Cylindrical cells; (b) Prismatic cells; (c) Pouch cells. Figure taken from [1]

2.1.1 Cylindrical Li-ion Cell

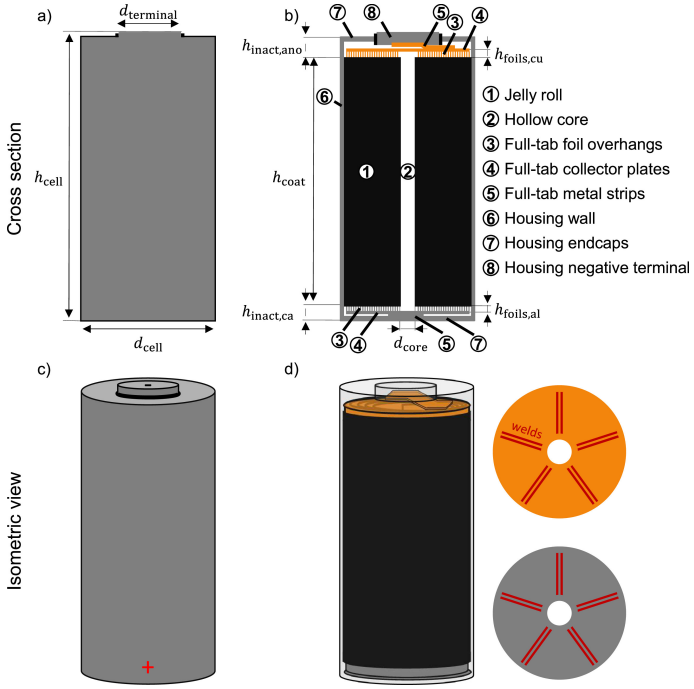

Figure 2.2: Simplified representation of a tab-less cylindrical lithium-ion cell employing a full-tab approach. Top section: a) Front view of the cell and b) sectional view with different components within the cell numbered from 1 to 8. Bottom section: c) Isometric view of the cell and d) figure depicting the position of tab plates. The venting mechanism has been omitted for clarity. Figure taken from [2]

A cylindrical lithium-ion cell consists of a protective metal casing (E.g. aluminium or steel) enclosing a jellyroll. The jellyroll is a tightly wound assembly of a positive electrode (cathode) made of E.g. LFP, NMC and a negative electrode (anode) commonly made of graphite. Separating these electrodes is a porous separator. The jelly roll in a cylindrical cell is wound around a pin and enclosed within a cylindrical cell casing, and in some instances, the pin or mandrel is absent. The presence of a mandrel contributes to added safety and mechanical strength to the cell [20]. Thin metal foils act as current collectors, which ensure electron flow while insulating rings and spacers maintain separation. Usually, the negative and positive active materials are coated on the current collectors. The anode has a copper current collector, and the cathode has an aluminium current collector. Tabs connect the electrodes to the external circuit, maintaining the current flow. The cell may include a vent mechanism for safety, and a cap seals the assembly.

Recently, cylindrical cells have garnered significant interest in terms of their design and production. This interest was generated after the release of the Tesla Model Y, which used 4680 battery cells. This cell has a volume that is 5.5 times greater than that of 21700 cells and 8 times more than that of 18650 (18 mm: diameter, 65 mm: length) cells. The design also aims to decrease the cell resistance. However, at the moment, despite the innovative tab design and increased energy per cell, it

does not show a notable advantage in terms of energy density when compared to its conventional counterparts [1]. The below figure displays a relative comparison of 4680 cell dimensions to the conventional 18650 and 21700 cylindrical cells.

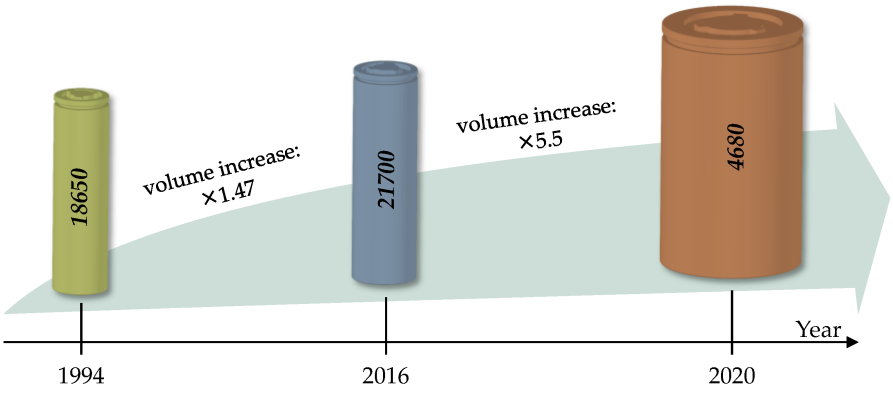

Figure 2.3: Evolution of cell formats. Figure taken from [1]

2.2 Material Characterization Techniques

2.2.1 X-ray Computed Tomography (XCT) Scanning

XCT is used to produce digital images of a sample's internal structure and imaged volume. For 3D modeling, the sample needs to rotate, and the distance to the X-ray radiation transmitter determines penetration, influencing image quality. XCT helps in identifying any defects that may have occurred while manufacturing the cell, any damage due to shock and vibration while transporting the cell from the supplier to the customer, any possible mechanical damages or swelling of the jellyroll, placement and alignment of different components within the cell, welding used for tabs onto the anode/cathode disk and number of tabs in the cathode and anode side [21]. It gives an overview of the cell design such as an estimate of the length of electrodes, whether a mandrel is being used (for cylindrical cells), information about the vent, etc. XCT scans give information about the density of the different components, thereby giving an idea of what that material may be.

2.2.2 Scanning Electron Microscopy (SEM)

Scanning electron microscopy is used for image sampling using a beam of electrons, producing results scaled to the nanometer range [22]. A filament is used to emit these electrons, which are subsequently focused into a beam. A set of lenses within the electron column are used to focus the beam on the test sample.

Various types of electrons, like backscattered electrons and secondary electrons, are produced after their interaction with the sample matter. This interaction between the sample surface and the electron beam generates an image from the emitted electrons (signals) of the scanned sample [22]. The backscattered electrons possess significant energy and lose a fraction of it upon reflection from the sample. They come from deep inside the sample, usually a few microns beneath the surface and strongly engage with the sample material. Through elastic interaction with the

sample, these offer compositional information with low-resolution images [23].

Secondary electrons are produced due to inelastic beam-sample interactions. They have relatively low energy and originate below a few nanometers of the surface of the sample, providing topographical information due to being sensitive to the surface, of the sample structure. The operator then adjusts the brightness and intensity of these signals to obtain a clear image on the viewing screen [22].

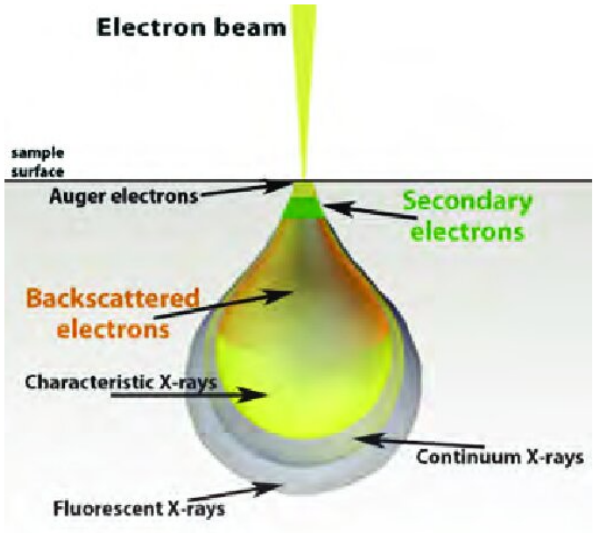

Figure 2.4: Varying electron penetration depths through the sample. Figure taken from [3]

2.2.3 Energy Dispersive X-ray Spectroscopy (EDX)

Energy Dispersive X-ray Spectroscopy is a powerful elemental analysis technique linked to electron microscopy, which uses X-rays, produced by the sample upon interaction with the electronic beam to identify the elements present in the test sample [24]. The electron beam is focused on a limited area of the sample, which makes it possible to map its surface elements. This is useful to understand the sample surface's atomic composition given in % atoms or to check for contaminants on the sample, if any.

2.3 Electrical Characterization Techniques

2.3.1 Electrochemical Impedance Spectroscopy (EIS)

EIS stands for Electrochemical Impedance Spectroscopy. It is a technique which is used to measure the impedance characteristics of an electrochemical system over a range of frequencies. When an oscillating voltage is applied to an electrochemical cell, it oscillates at an angular frequency of ω and the corresponding current response has an angular frequency of ω along with a phase shift Φ. Analogous to an electrical circuit, this phase difference is caused due to components such as capacitors and inductors.
Impedance (Z) consists of two different components: a real "resistive" part (Z') and an imaginary "reactive" part (Z''). The real part is an analog of resistance in a DC

system, whereas the imaginary part is due to the AC excitation, which will cause an oscillating component.

$$Z = Z' + iZ'' \tag{2.1}$$

An expression similar to Ohm's law helps in calculating the impedance of the system as

$$Z = \frac{E_\mathrm{t}}{I_t} = \frac{E_0 \sin(\omega t)}{I_0 \sin(\omega t + \phi)} = Z_0 \frac{\sin(\omega t)}{\sin(\omega t + \phi)} \tag{2.2}$$

Impedance is therefore expressed in terms of a magnitude, Zo, and a phase shift Φ.

The fundamental principle of the EIS testing involves applying either a sinusoidal current (Galvanostatic EIS) or voltage (Potentiostatic EIS) to the cell and measuring the resulting characteristic response, which is dependent on the cell's impedance (Z) and the phase angle Φ [25]. The application of this technique helps to characterize different processes evolving within the cell [26]. Furthermore, it is known as a non-destructive and dependable method capable of pinpointing the source of cell degradation processes and revealing certain aging effects that are challenging to detect using conventional testing methods [27].

Any fluctuation in the magnitude of different parameters such as current, SOC (State of Charge), voltage and temperature can influence the impedance and consequently the resultant EIS curve. The real and imaginary parts of the impedance are usually represented in what is called as a Nyquist plot which is a complex plane having the real part of the impedance (Z_{real}) in the x axis and the imaginary part of the impedance (Z_{imag}) plotted on the y axis. In the plot the points corelate to a particular frequency. A Bode plot is also used to represent the phase and magnitude of the impedance in the y axis with corresponding frequency in the x axis.

Classical EIS tests need to fulfill four criteria [28]:

1. Linearity: In response to the applied signal, the resulting signal must show a linear response.
2. Stability: The electrochemical system must remain stable over time and should revert to its original state without any fluctuations once the applied signal is stopped.
3. Causality: The response signal must be caused by and must be only dependent on the applied signal.
4. Finiteness: The impedance values must be finite over the entire frequency range. The system, at any frequency, should not define infinite or undefined impedance values.

2.3.1.1 Equivalent Circuit Models (ECM's)

An approach to evaluate the impedance data is to model the system being investigated, using an equivalent circuit (EC) method. This model basically tries to simulate the experimental response received from the system with a signal resulting from an electrical circuit using a combination of electrical components like inductors, resistors and capacitors. The Nyquist plot is split into three regions: namely the

ohmic region (frequency above 1 kHz), the Mid-frequency region (frequency interval between 1000 Hz and 0.1 Hz) and the low-frequency region (frequency lower than 0.1 Hz) [26].

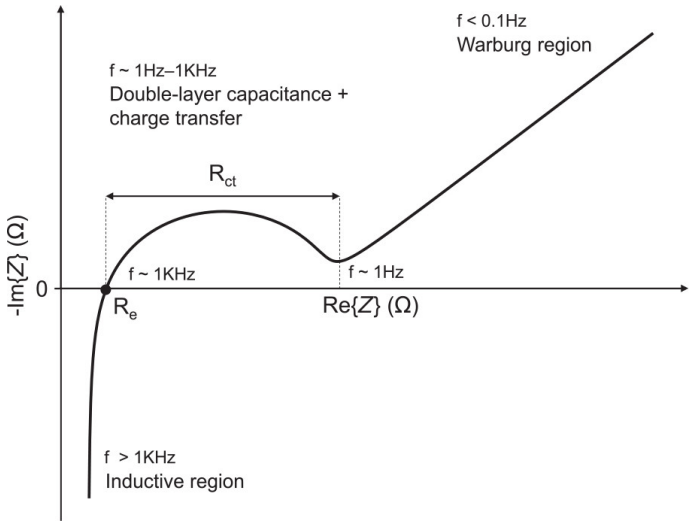

Figure 2.5: Typical Nyquist plot for a Li-ion cell. Figure taken from [4]

Some elements and equivalent circuit models are mentioned below.

Warburg (W) element: This element describes the diffusion mechanism at low frequencies. Several models of the Warburg element are found depending on the conditions governing the problem [26].

Figure 2.6: A single Warburg element

Constant Phase Element (CPE) and Double layer capacitance (C_{dl}): The contribution of the double layer is represented by C_{dl}. The CPE element accounts for the double layer's non-ideal behavior, which differs from that of the capacitance. It is used to explain the dispersion effect and operates similarly to a capacitor when its exponent is equal to 1, and resistance characteristics are indicated when its exponent is equal to 0 [26]. It is represented by 2.3 [29].

$$Z_{CPE} = \frac{1}{jC(\omega)^n} \tag{2.3}$$

Where, C represents the value for double layer capacitance, ω the frequency and the factor n varies between 0 and 1.

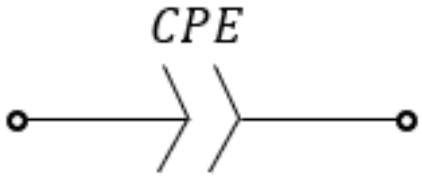

Figure 2.7: A single CPE element

Randles Circuit: This circuit (Figure 2.8) consists of R_e (the resistance resulting from the electrodes, the electrolyte and current collectors, etc.) in series with a parallel connection comprising of R_{ct} (the estimated resistance corresponding to the faradaic reaction), the Warburg element and a CPE. If the Warburg element is removed from the circuit, a so-called simplified Randles circuit (Figure 2.9) is obtained. [30, 31]

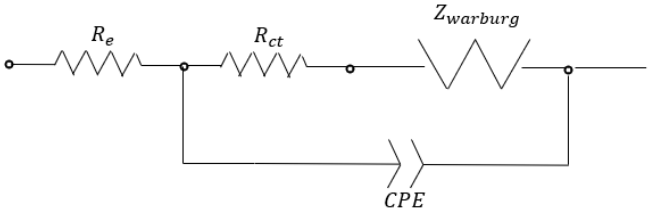

Figure 2.8: Randles circuit

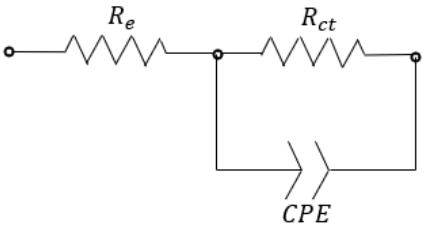

Figure 2.9: A simplified Randles circuit with CPE in parallel with R_{ct}

2.3.2 Charge & Discharge of a Li-ion Cell

Charging and discharging in cells are done using galvanostatic/constant current (CC) and potentiostatic/constant voltage (CV) cycling methods. In both of these methods, either a constant current or a constant voltage is applied to the cell until a specified limit is triggered. In the CC method, voltage is used as the limit, whereas in the CV method, current is the limit. Time can also be used as one of the limits in combination with the aforementioned limits. For this thesis, in the CC step, a constant C-rate is applied, until a set voltage limit is reached. A charging rate of 0.5 C means that the cell will be charged in 2 hours (120 minutes), while a rate of 1 C would mean the cell will be charged in an hour. If the cell is undergoing CC-CV charging, then the C-rate and cut-off voltage limits are set for the test. The cell

is then charged at that particular C-rate until the cut-off voltage is reached, after which the test is switched to CV charging. The CV step ensures that the cell reaches full charge. Figure 2.10 represents an example of a CC-CV profile.

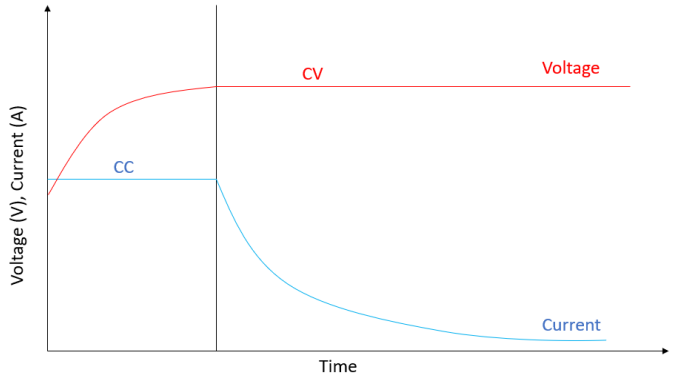

Figure 2.10: An example of CC-CV profile

2.3.3 Current Pulse Method

In this method, the DCIR of the cell during charge or discharge using a CC pulse is evaluated by monitoring the voltage profile. Figure 2.11 represents an example of such a profile. This resistance is calculated using Ohms law given by:

$$R_{\Omega} = \frac{|V_1 - V_2|}{|I_1 - I_2|} = \frac{|\Delta V|}{|\Delta I|} \tag{2.4}$$

Here, suffix 1: is the time at which the pulse is applied, and suffix 2 is: the time at which the resistance is measured.

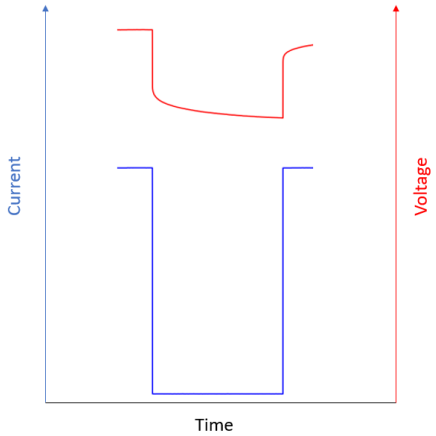

Figure 2.11: Voltage and current profile

2.3.4 Reference Performance Test (RPT)

The Reference Performance Test (RPT) is performed at a certain temperature to test the state of health (SOH) of the cell and can also involve different tests to assess the capacity and internal resistance of the cell. Cell capacity is assessed using

CC-CV charge and discharge until the cell reaches the minimum voltage provided by the cell manufacturer. The resistance is determined through Ohm's law after applying a specific current pulse for a defined period.

This test is non-destructive, and it is supposed to not expose the cells under test to extreme conditions while characterizing their kinetic and thermal changes [26]. The cell's capacity is determined at C/3 (discharge in 3 hours) rate and can be followed by pulse tests, which are done to determine the DCIR of the cell. Similarly, more steps could be added (for example, EIS test) to such a protocol, depending on what the area of interest is for the particular cell.

2.3.5 Rate Capability Test (RCT)

The rate capability test is performed to evaluate the change in capacity of the cell as a function of C-rate. These tests compare the cell's capacity at various C-rates and temperatures to assess its performance. By examining the capacity variations across different C-rates, the RCT provides information about the cell-internal resistance and its impact on overall performance.

This test is done to analyze the capacity retention, voltage profile during charge & discharge and thermal performance of the cell at high and low C-rates [32]. These tests are also done to understand if there is any discrepancy between the current limits from the manufacturer to the actual limits of the cell [33].

3

Experimental Set-up

In this section the tools and methods used to perform cell teardown, characterization of the harvested material and electrical characterization of the cell have been described.

3.1 Test Object (TO)

A commercial-grade, large-format 4680 Li-ion cylindrical cell from BYD has been used throughout this thesis work. The positive and negative electrodes of the cell are LFP and graphite, respectively. Pictures of the cell are given in Figure 3.1.

Figure 3.1: Figure depicting the positive and negative terminals of the T.O

Parameter	Values
Capacity at 0.5C	15.3 Ah
Max charge voltage	3.6 V
Discharge end voltage	2.0 V

Table 3.1: Capacity and voltage values for the T.O

3.2 Cell Teardown Process

To examine the various components within the cell, several test objects were opened in an argon-filled glovebox, ensuring an inert atmosphere. The dimensions of specific components, such as the anode, cathode and separator were measured, including the anode overhang. Further characterization of these components were conducted to understand key aspects such as the material used for the cathode, anode & separator, the thickness of the active material coating on the electrodes, and the particle sizes of the cathode and anode.

3.2.1 Preparation for Cell-Teardown

Before the test object undergoes teardown in the glove box, it has to be prepared for the process. The preparation involves two steps and they are highlighted below:

3.2.1.1 X-ray Computed Tomography (XCT) Scanning

- In this study, an XCT scan was done for the cell. The scans were compared to the teardown images of the BYD cell. The XCT machine is from RX Solutions brand and operates using XAct software, with additional post-processing capabilities provided by VgStudio.
- The X-ray source in the machine can operate at 110, 130 or 150kV (upto 230kV) with a Cu filter and has a maximum sample size capacity of 350 x 500mm. The finalized scans are processed and segmented using the myVGL software by VOLUME GRAPHICS.

3.2.1.2 Cell Discharge

Before the teardown, the cell was discharged to 0% SOC to minimize the consequences due to short circuits during the cell-opening process within the glovebox. The TO was discharged at C/3 and 25°C until the minimum voltage corresponding to 0% SOC was achieved represented by Table 3.1.

3.3 Cell-Opening Methodology

This section will highlight the two different work methodologies explored while preparing the cell for its opening. Both methods employ a glove box to retrieve the jelly roll from the cell.

3.3.1 Glove Box Setup

The glovebox model used for this thesis is a GS Mega manufactured by Svenska Labex AB. Ideally, the O_2 and H_2O levels must be lower than 1 ppm [34].

3.3.2 Method 1: Using hand tools (Plier and Wire cutter)

This method involves opening the cell entirely within the glove box using only hand tools, such as various types of pliers and wire cutters.

- The green plastic film (shrink sleeve) covering the cell housing is gently peeled off with pliers and sharp ceramic tweezers. The insulation ring as shown in Figure 3.2, positioned to avoid short circuits with the outer can, is also removed. The cell is then secured in a holder to continue with disassembly.

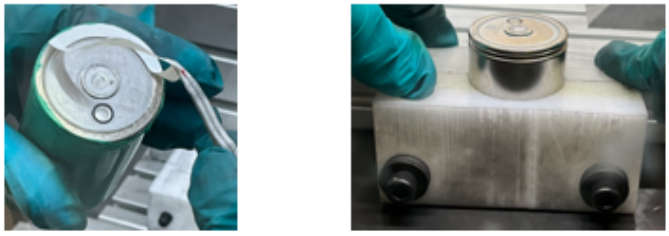

Figure 3.2: Removing the insulation ring with ceramic tweezers and mounting the cell on the jig for teardown

- The cell casing is cut just below the positive terminal (cathode) using a hand-held pipe cutter, carefully revolving it along the crimp. This cutting position was determined using the XCT scan. The metal housing cap is then opened around the crimp, as shown in Figure 3.3.

Figure 3.3: Using a pipe cutter the positive cap as seen in Figure 3.1 was opened to reveal the plastic ring separating the Al tabs from the casing

- After opening the positive cap, a plastic pipette was inserted into the hollow mandrel for sampling any possible electrolyte. This was sealed in a vial for further analysis.

Figure 3.4: Plastic pipette being used to collect any possible electrolyte

- After removing the cap, small notches were made around the circumference of the open part of the casing using a wire cutter, as depicted in Figure 3.5. This weakens the casing, making it easier to open with pliers in the next stage.

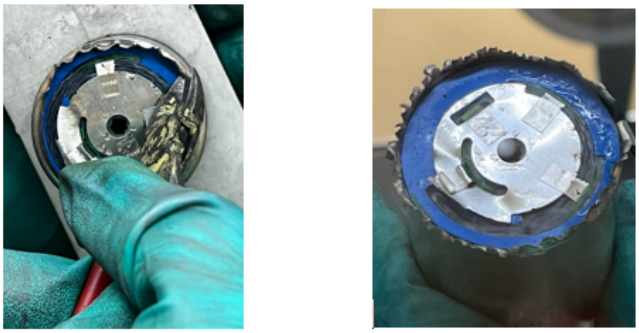

Figure 3.5: Wire cutter being used to create notches

- After creating the notches, a long nose plier was used to pull down on one of the notches. If the notches are too large, the plier may not be able to grip them effectively due to their structure.
- Once the plier securely grips on a notch, it is twisted and rotated outward to strip the steel casing, as shown in the figures below.

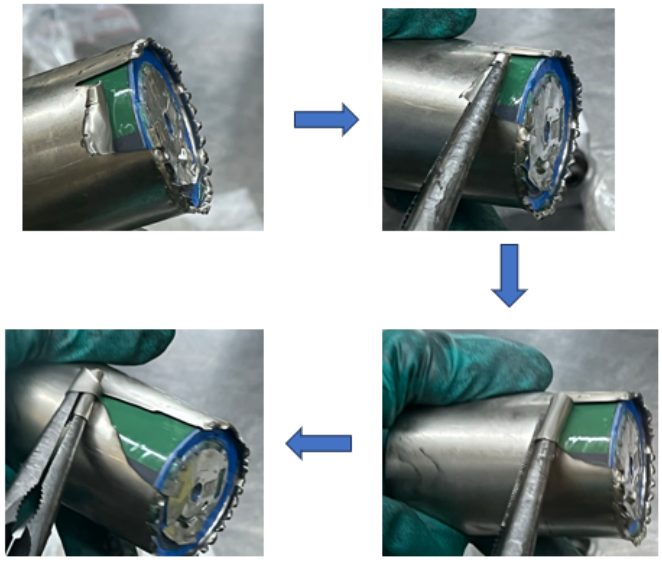

Figure 3.6: Long nose plier being used to strip off steel casing

- The cell casing is very weak at this point, and it can be pulled wide apart by bending and splitting the steel can open with hands.

Figure 3.7: Retrieved jellyroll from the casing

3.3.3 Method 2: Using a combination of power and hand tools

This method involves scoring the cell casing outside the glove box to facilitate easier opening once placed inside the glove box. The cell was scored using a power-cutting tool, a Dremel 8260. The detailed explanation of this method is described below.

- The discharged cell is held in a customized 46xx series holder jig. This is done so that the jig can be mounted on a bench vise to hold it in place.

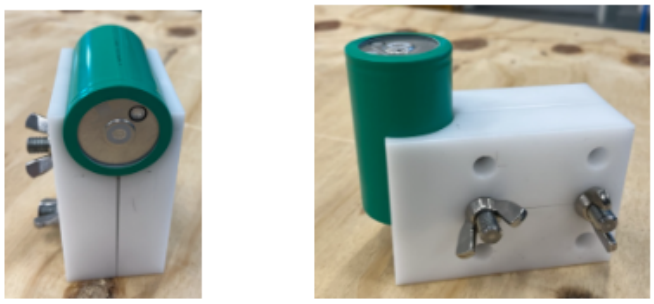

Figure 3.8: The BYD-4680 cell being held in a customized 46xx series holder

- Once the jig is mounted, the outermost green plastic film is removed using a Dremel tool. Then, a long incision is made along the outer steel casing.
- This process is repeated on the opposite side of the cell, and an additional incision is made at the bottom of the cell.

Figure 3.9: Outer insulation plastic tape being cut, longitudinal and bottom incisions are being made using Dremel tool

- The cell is then introduced inside the glovebox where a ceramic knife is used to follow the path created by the Dremel tool, effectively cutting it open, as illustrated in the figures below.
- This retracing action using the ceramic knife is done on both sides to further weaken the casing.

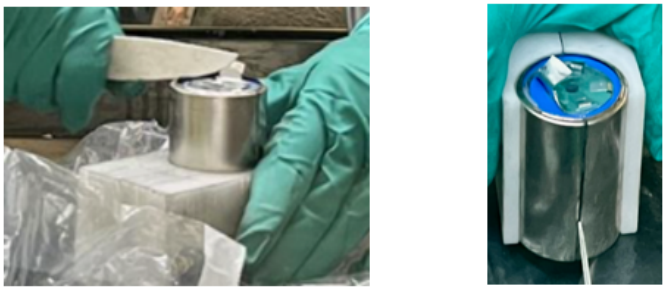

Figure 3.10: Ceramic knife being used to cut an incision at the crimp and cut along its length

- After this step, the cell casing is pulled wide apart by bending and splitting the steel can open with hands. Pliers could also be used to take this action.

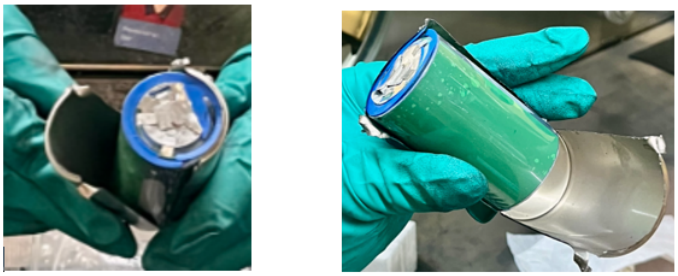

Figure 3.11: Cut open steel casing being pulled wide apart to free the jellyroll

3.4 Cell Component Characterization

This section outlines how the jellyroll extracted from the cell is unwound, detailing the opening of various jellyroll components for material and geometrical characterization. Table 3.2 shows the different instruments used for characterizing the cell.

3.4.1 Geometrical Characterization

- A ceramic tweezer was used to carefully remove the green outer film as seen in Figure 3.11 from the jellyroll before unrolling its electrodes. Figures 3.12 and 3.13 depict how the separator and electrodes were measured using a steel ruler, respectively.

Tools and Equipment Used for Different Cell Characterization		
Cell-Opening	**Geometrical Characterization**	**Material Characterization**
Bench vise	Vernier caliper	Plastic pipette
Dremel tool	Ruler	SEM/EDX
Cell-holder		Cold mounting resin (2K epoxy)
Pipe cutter		DSC
Ceramic knife		NMR
Wire cutter		GC-MS
Ceramic tweezers		ATR-FTIR
Long nose pliers		

Table 3.2: List of tools and equipments used throughout this thesis work

Figure 3.12: Ruler being used to measure the length of the separator

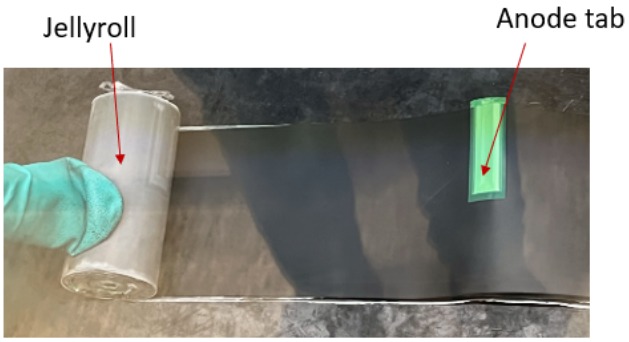

Figure 3.13: Jellyroll being unwound for measuring the length of electrodes

- As shown in Figure 3.13, the length of electrodes were measured using a ruler, after which the electrodes and separator were wound over plastic and metallic pipes covered with an insulating film, depicted by Figure 3.14.

Figure 3.14: Cathode, separator, and graphite anode being wound over cylindrical tubes, respectively

3.4.2 Material Characterization

Samples of the positive electrode, negative electrode, tabs and separator were extracted from the roll for this analysis. The objective was also to identify the primary chemical components.

Material characterization was conducted using Scanning Electron Microscopy (SEM) and Energy-Dispersive X-ray Spectroscopy (EDX) with a JSM-IT300 instrument (JEOL, Japan). The plastic components, including the mandrel and discs, were analyzed using Differential Scanning Calorimetry (DSC) with a Mettler Toledo Thermal Analysis System DSC 3+ STARe System. Additionally, Attenuated Total Reflectance Fourier Transform Infrared Spectroscopy (ATR/FTIR) was performed using a Bruker VERTEX 70v FT-IR spectrometer equipped with a Pike Technologies MIRacle single-reflection diamond ATR sampling accessory. However, a detailed explanation of the working principle and an in-depth discussion of the results, for ATR-FTIR, DSC, GC-MS and NMR fall outside the scope of this thesis.

3.4.2.1 Sample preparation for material composition analysis

- Small samples of the cathode, anode, anode tabs and separator were retrieved from the jellyroll for SEM analysis.
- These samples were washed three times with Dimethyl Carbonate (DMC). Care was taken to avoid contaminating the electrodes or the tab, using tweezers and tissue paper.
- After washing the samples, they were dried by holding and waving them in the glove box using a ceramic tweezer.
- After drying the samples, they were stored in small plastic zip bags and were taken out of the glove box via the antechamber.
- These samples were placed in a holder, which was later placed inside the Scanning Electron Microscope.

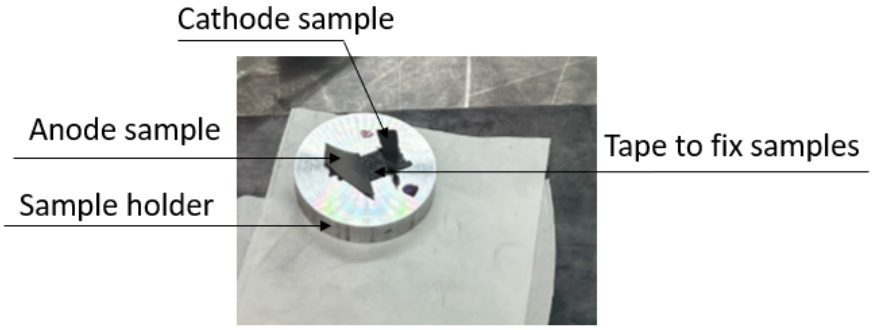

Figure 3.15: Holder containing electrode samples for SEM and EDX analysis

3.4.2.2 Sample preparation for cross-sectional thickness

This section describes the process of using epoxy to mount different electrode samples and assess the thickness of the active material and current collectors. It consists of the following steps:

- The electrode samples, along with the separator, are cut in an approximately 2 cm × 2 cm square shape to hold them on fixation clips to be placed inside the mould.

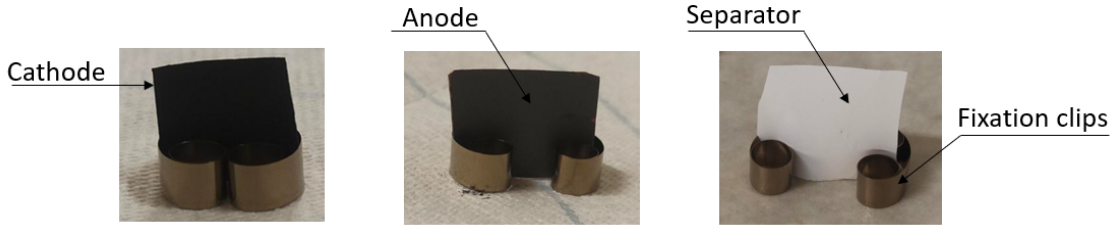

Figure 3.16: Positive electrode, anode and separator held in fixation clips

- The mounting was done using a cold-curing resin based on two-fluid epoxy components (Epofix). The setting time for EpoFix is approximately 12 hours.
- A plastic mould was used to house the collected samples which was then cured in a vaccum CitoVac impregnation unit for approximately 12 hours [35]. It was then polished using a Struers LaboForce-100 equipment consisting of magnetic discs for grinding and polishing specimens.

Figure 3.17: Epoxy cast removed from the plastic mould

3.5 Electrical Characterization

This section highlights the methods and processes used to perform different electrical performance tests. These tests were performed using a four-point measurement setup [36].

3.5.1 Test aparatus

The tests were performed in a thermostatic chamber equipped with battery cyclers. Figure 3.18 illustrates an air-cooled cylindrical cell holder from Arbin which has been used to hold the cell and connect it to the electrical testing equipment. K-type thermocouples were positioned at the two ends to measure temperatures at the positive and negative terminal. Another sensor was positioned at the center of the cell to measure the temperature of the center body. Two PT-100 sensors were used to measure the ambient temperature around the cell.

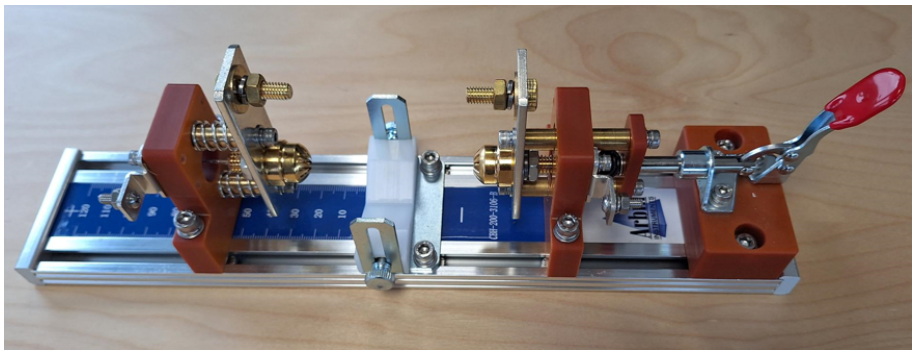

Figure 3.18: Jig used for electrical testing

3.5.2 Reference Performance Test (RPT)

The discharge capacity at 25°C was obtained by charging the cell at C/3 until 3.6V followed by a CV phase at a C/20 cutoff current and then discharging the cell at C/3 until 2.0V. Additional charge and discharge sweeps at C/25 were performed to register the pseudo OCV curves. A series of CC discharge pulses of 10 seconds was applied to the cell at different % SOC (10%, 30%, 50%, 70% and 90%, thereby discharging the cell), and their corresponding internal resistance was evaluated as described in Section 2.3.3.

3.5.3 Rate Capability Tests (RCTs)

RCTs were performed at 25°C for different discharge C-rates (C/5, C/3, C/2, 1C, 2C) and -10°C for C-rates (C/5, C/3, C/2, 1C). The discharges at -10°C were always performed following a charge at 25°C to minimize the risk of lithium plating.

3.5.4 Electrochemical Impedance Spectroscopy (EIS)

GEIS was performed using a potentiostat/galvanostat Gamry Reference 3000 connected to a Reference 30K Booster, in the range 100kHz - 0.1Hz and at different SOCs. The test was done at 0%, 10%, 30%, 50%, 70%, 90% and 100% SOC reached upon charging and discharging the cell stepwise with coulomb counting. The resting time for maximum and minimum SOCs (100% and 0%) was chosen to be 120

minutes, and 60 minutes for intermediate SOCs (10%, 30%, 50%, 70% and 90%). The setup used to perform the test is shown in Figure 3.19. The Python package impedance.py was used to fit the EIS data to an ECM to estimate the R_{ct} [37].

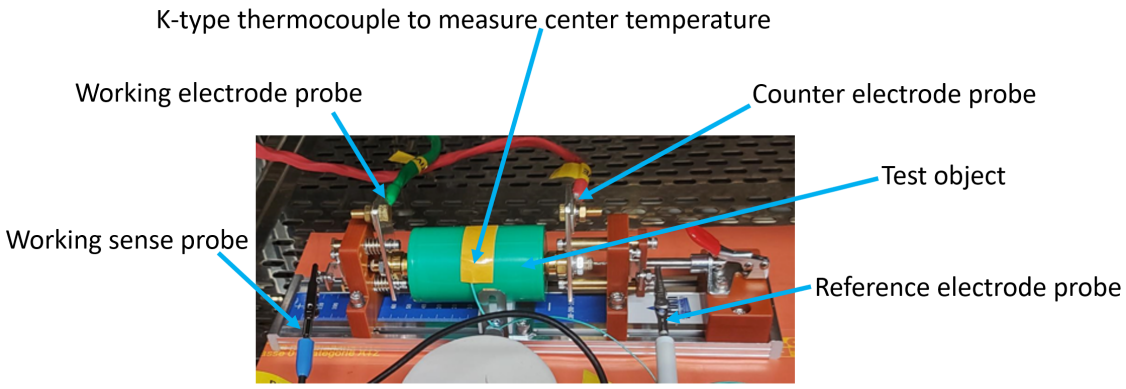

Figure 3.19: EIS test setup for the cylindrical cell

4

Results and Discussion

This section is structured as follows:

1. The first part focuses on the comparison of cell opening methodologies that have been implemented and on their optimization.
2. The second part discusses the results from the material analysis while also characterising the different components of the cell comparing teardown images with their XCT images.
3. The final part provides results from the various electrical tests performed on the cell, as detailed in Sections 2.3 and 3.5.

4.1 Optimization of Cell Opening Methodology

This section highlights the different pros and cons identified while using different cell-opening methodologies and explains the development of equipment that could be used to open any-format cylindrical cell:

4.1.1 Method 1: Using hand tools (Plier and Wire cutter)

4.1.1.1 Advantages

- The user can maintain control over the tools to open the casing, thereby being cautious not to damage the jellyroll or the gloves while stripping away the steel.
- The electrolyte is collected after the top cap is opened using a plastic pipette, thereby mitigating any risks of electrolyte spillage.

4.1.1.2 Disadvantages

- Moving hands inside the glovebox becomes difficult when dealing with pliers and wire cutters in quick succession.
- The presence of so many notches on the surface raises safety risks associated with damage to the gloves in the glove box.
- The long nose pliers tend to frequently get wrapped around by the steel chips, making it difficult to open them after each attempt.
- The success of this procedure highly depends on the operator's expertise and skill.

4.1.2 Method 2: Using a combination of power and hand tools

4.1.2.1 Advantages

- The steel casing of the cell could easily be penetrated using a fiber disc-cutting tool.
- There is no strain on the hand since it can be done outside the glovebox.
- The Dremel tool produces a precise and clean cut on the surface without any notches. This prevents any possible damage or cuts to the gloves in the glove box.
- Once the cell is traced using the Dremel, cutting the steel casing using the ceramic knife is relatively easier.

4.1.2.2 Disadvantages

- The depth of cut cannot be accurately assessed before cutting the cell casing, which may lead to electrolyte spillage, posing multiple risks such as corroding and damaging the tools being used.
- The vapor from the spilled electrolyte is harmful when inhaled, and contact with the skin can be damaging if gloves are not worn.
- This also poses a risk to the jellyroll inside the casing, potentially causing cuts on its outer surface, exposing it to the atmosphere, thus contaminating and damaging the sample.
- The absence of pre-traced paths along the length of the cell makes it difficult to hold the Dremel tool steady, causing it to slip on the surface of the casing.

4.1.3 Using a novel Universal Cylindrical Cell Cutting Jig

A more efficient methodology can be implemented to enhance the cell-opening process. The following is a design proposal for novel equipment.

A jig with multiple fixed bases can be developed to secure the position of the cutting tool and control the movement of the cell being opened. To address the drawbacks of the methods described in Sections 4.1.1 and 4.1.2, the primary feature should be depth control to prevent damage to the jellyroll inside the cell casing. A Dremel tool equipped with an adjustable depth control ring on its cutting disc can be mounted on the jig. The depth control ring, which can be set to the desired cutting depth, will be placed on the cutting tool shaft, acting as a stopper. This provides greater control to the user, preventing the disc from penetrating deeper than the pre-set depth, thereby protecting the jellyroll.

Using a power-tool such as a Dremel allows easy penetration of the steel can, scoring the surface with a clean and precise cut without any notches. Additionally, a flexible cell carriage can be designed to hold various formats of cylindrical cells. This carriage, positioned on guide rails, provides a stable base for the cell, ensuring it moves only axially under the cutting tool, controlled by a hand knob attached to the carriage. This setup might improve precision and safety in the cell-opening process by preventing the cutting disc from slipping onto the surface of the casing.

4.2 Material Analysis and Component Characterization

This section comprises further steps in the teardown process, where different components of the jellyroll are harvested for material and geometrical characterization. The observations from the analysis are described further in this section.

Cathode Side	**Details**	**Method/Tools**
Disc tab dimension	O.D 3 cm; I.D 0.6 cm; Welded tab-width 1.1 cm	Caliper
Disc tab composition	Aluminium	SEM-EDX
Tab dimensions	3.2 cm × 0.5 cm	Ruler
Tab composition	Aluminium	SEM-EDX
Cap composition	Aluminium	SEM-EDX
Number of tabs	4	Visual inspection
Tape on the tab - dimensions	5 cm × 4 cm	Visual inspection
Tape without the tab (Fig. 4.4)	3.8 cm × 3.1 cm	Ruler
Tape on current collector tab	3.6 cm × 1.5 cm	Ruler
Tape on the tab composition	Polypropylene terephthalate	ATR / FTIR
Cathode composition	Ti, Fe, P, C	SEM / EDX
Cathode morphology	Spherical	SEM
Current collector thickness	17 μm	SEM
Cathode thickness	149 μm	SEM
Tape on the coating (in correspondence to anode tab)	6	Visual inspection
Cathode length	513 cm	Ruler
No. of tapes on Cathode	10	Visual inspection

Table 4.1: Detailed specifications and measurements on the cathode side

Anode Side	**Details**	**Method/Tools**
Disc tab dimension	O.D 3.8 cm; I.D 0.6 cm; Welded tab width 0.6 cm	Caliper
Disc tab composition	Cu, Ni	SEM-EDX
Tab dimensions	3.7 cm × 0.6 cm	Ruler
Tab composition	Ni	SEM-EDX
Number of tabs	3	Visual inspection
Tape on the tab - dimensions	3.6 cm × 1.5 cm	Ruler
Tape on the tab composition	Polyethylene terephthalate	ATR-FTIR
Anode composition	Carbon	SEM / EDX
Anode morphology	Flaky	SEM
Anode current collector thickness (Cu)	10.6 μm	SEM
Anode thickness	116 μm	SEM
Anode No. of tapes	3	Visual inspection
Anode length	526 cm	Ruler
Anode overhang (anode and cathode length comparison)	13 cm	Ruler
Anode overhang (anode and cathode width comparison)	2 mm	Ruler

Table 4.2: Detailed specifications and measurements on the anode side

Parameter	**Details**	**Method/Tools**
Separator Composition	Polypropylene	ATR-FTIR/DSC
Separator Dimensions	1080 cm × 7.3 cm	Ruler
Hollow Mandrel Dimensions	ID-0.5 cm, OD-0.7 cm, Length-7 cm	XCT, Ruler, Caliper
Hollow Mandrel Composition	Polypropylene	ATR-FTIR
Electrolyte Composition	EC, EMC, DMC, $LiPF_6$	GC-MS, NMR

Table 4.3: Detailed specifications and measurements for separator, mandrel and electrolyte

Component	Details	Method/Tools
Blue isolator disc dimension	O.D 4.4 cm; I.D 0.6 cm	Ruler, Caliper
Blue isolator disc composition	Polypropylene	ATR-FTIR
Can Wall Thickness	0.7 mm	Caliper
Green film on electrodes composition	Polyethylene terephthalate (PET)	ATR-FTIR
Green film covering the outer jellyroll	12 cm × 7 cm	Ruler
White gasket at positive cap (Fig. 4.15)	Polypropylene	ATR-FTIR

Table 4.4: Polymer Component Details

4.2.1 Cathode

The SEM images are shown in Figure 4.1, where the cathode particles display a spherical morphology. EDX analysis performed on a section of the cathode revealed the presence of carbon, oxygen, phosphorus, iron and a small amount of titanium (0.2 atomic%). Thus confirming the cathode to be LFP.

This titanium doping might have been implemented to enhance the conductivity of the LFP cell [38]. From EDX analysis, the cathode tab was found to be made of aluminium. Table 4.1 summarizes the cathode specifications.

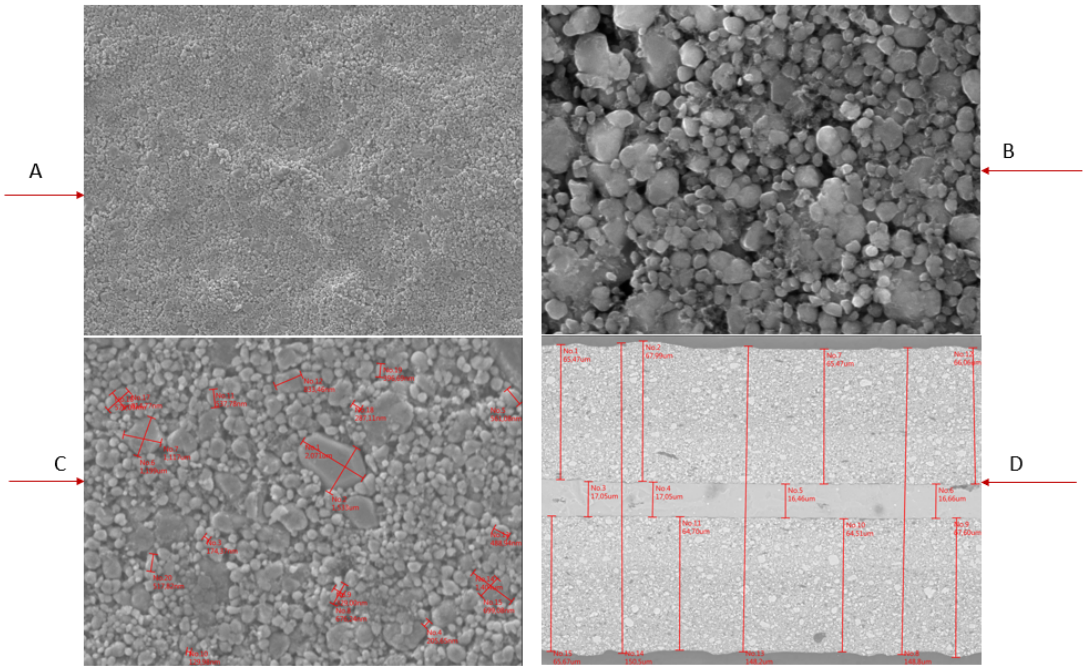

Figure 4.1: SEM images of the cathode. Top section: A) 3K magnification and B) 14K magnification. Bottom section: C) 10K magnification highlighting particles with dimensions ranging from 0.2-1.5µm and D) cross-sectional thickness of the aluminium current collector and the active material

During teardown of the cathode roll, an aluminium tab (Table 4.1) was observed to be welded to the aluminium current collector. This tab is positioned between two narrow layers of green PET film. Essentially, the aluminium tab and the current collector layer are enclosed between plastic films on both sides, as indicated by the red arrows in Figure 4.2.

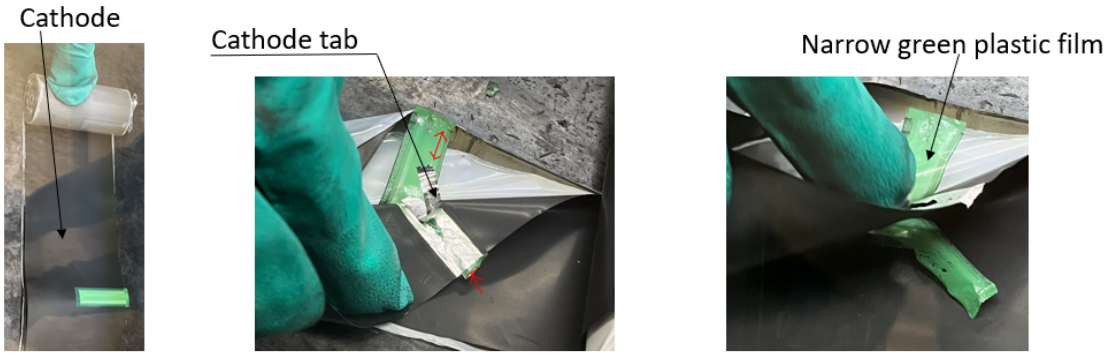

Figure 4.2: The green PET film along with the aluminium layer and cathode tab can be seen

The narrow green plastic film, whose width as depicted by the blue line, is attached to the cathode tab, and the impression of the anode tab can be seen on the broad green PET film at the edge of the cathode in Figure 4.3.

Figure 4.3: Broad and narrow green plastic films on the cathode side

Additionally, this PET film might serve to protect the cathode from the sharp edges of the nickel anode tab. During winding of the jellyroll, these films mark the relative position of the anode tab to the cathode. Therefore, an additional layer of film protection is placed on both sides of the cathode in this position to protect it from potential damage from the anode tab, thus preventing any burr defects or possible short circuits on the cathode as depicted in Figure 4.4.

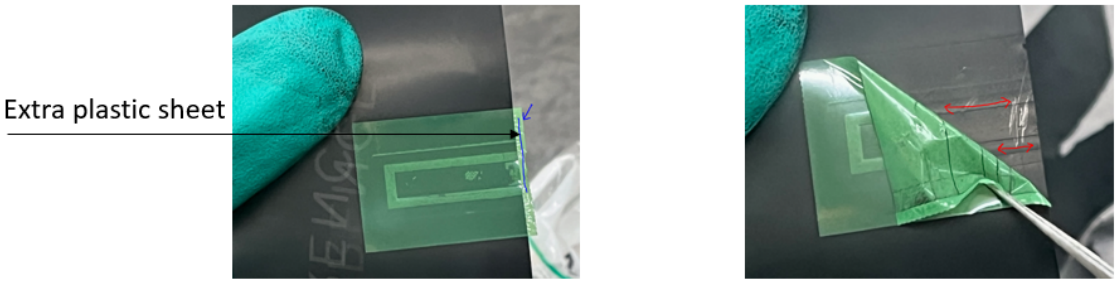

Figure 4.4: Broader PET film being used on the cathode relative to the anode tab position

The tiny extension of the PET film shown by the blue line in Figure 4.4 may provide extra protection to avoid any possible electrode contact. An impression of the anode tab can also be observed, portrayed by the red line in the above figure.

4.2.2 Anode

The SEM images of the anode are shown in Figure 4.5, where the anode particles display a somewhat flaky morphology. The presence of carbon from Table 4.2 confirms graphite being used as the anode. It was found to be 5.26 m long, which is longer than the 3.4 m long anode of the Tesla 4680 cylindrical cell [5]. EDX analysis revealed that the anode tab material is made of nickel. A detailed table characterizing the anode is provided in Table 4.2.

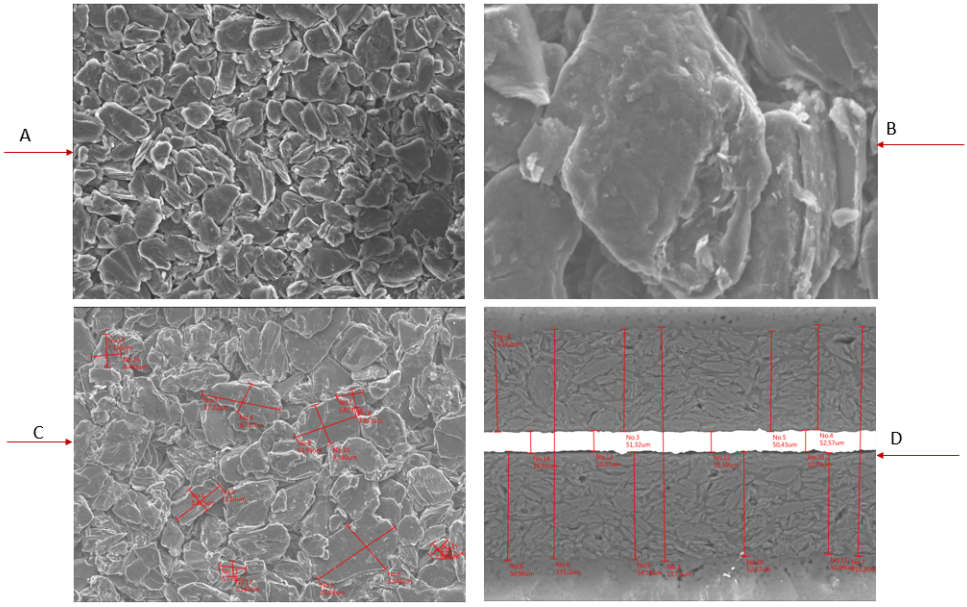

Figure 4.5: SEM images for the anode surface. Top section: A) 1K magnification B) 8K magnification focusing on a specific particle. Bottom section: C) 10K magnification highlighting particles with dimensions ranging from 3.2-20µm and D) cross-sectional thickness of the copper current collector and anode

During teardown, for the anode roll, a thin green plastic film is observed to be taped over the anode tab, indicated by the red line in the figure. The blue line highlights

the impression of the plastic film covering the cathode tab on the anode as shown in Figure 4.6.

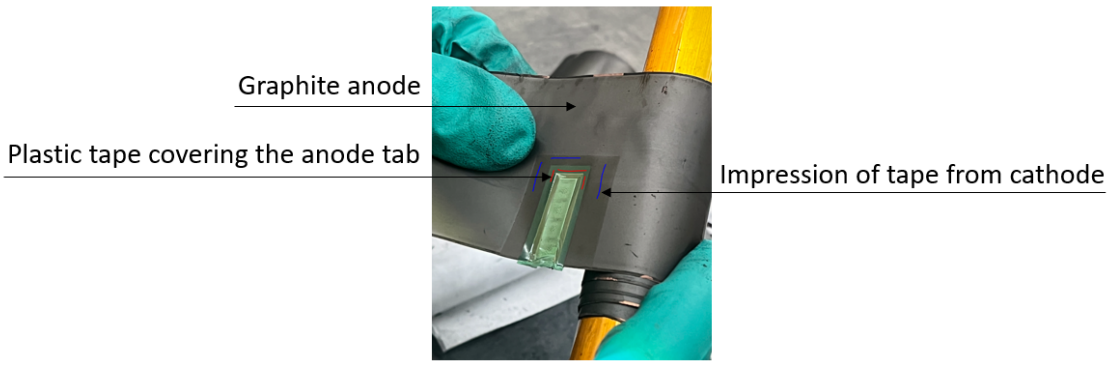

Figure 4.6: Observation on anode

The nickel tab is welded to the copper foil sandwiched between the tab and another narrow layer of green plastic film. So, the nickel tab and the copper layer are sandwiched between plastic films on either side, as seen in Figure 4.7.

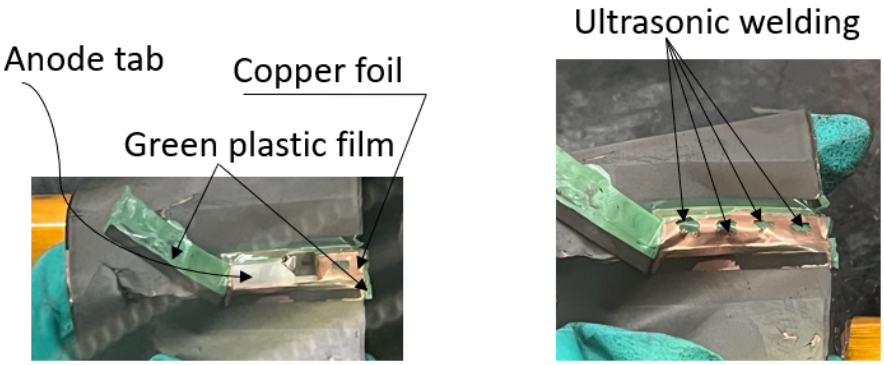

Figure 4.7: The copper layer sandwiched between the tab and narrow green plastic film

Upon removing the Ni tab from the anode, four distinct pyramid pattern spots indicating an ultrasonic weld can be observed. These spots are highlighted with blue arrows in Figure 4.8.

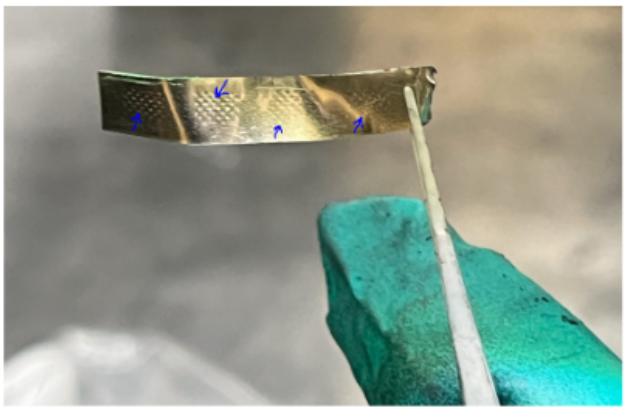

Figure 4.8: Ultrasonic weld spots seen on anode tab

The Cu current collector is coated with anode, that is, graphite (Table 4.2), binder, etc. appearing thin, brittle, and coarse. In contrast, the Al current collector, coated with LFP (Table 4.1), is relatively thick, strong, and smooth, as seen in Figure 4.9.

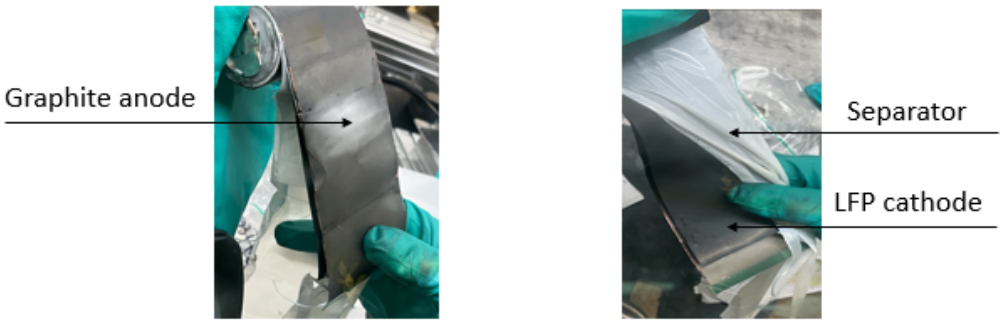

Figure 4.9: Observations on cathode, anode and separator

4.2.3 Separator & Electrolyte

From SEM-EDX analysis, the separator is primarily composed of carbon (98%) with a small amount of oxygen (2%). However, further FTIR analysis proved that the separator is made of polypropylene, as also mentioned in Table 4.3.

During teardown, the green plastic film (Table 4.4) covering the separator is initially removed while unrolling the jellyroll. The separator was found to be 10.8 m long, which is much longer than the 7.3 m long separator of the Tesla 4680 cylindrical cell [5]. Additionally, no ceramic coating was found on the separator. Two overlapping separator openings that begin at different locations are observed. One separator is positioned above the anode, while the other is below the anode, as shown in Figure 4.10. The electrolyte is composed of EC, EMC, DMC and $LiPF_6$. Information about mandrel and electrolyte composition are summarized in Table 4.3.

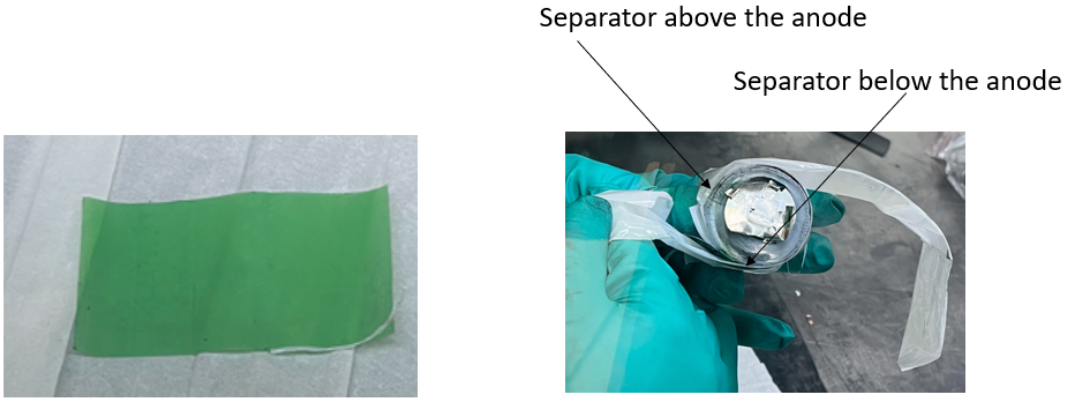

Figure 4.10: Green plastic film and the two distinct separator beginning locations

The separator appears as a continuous sheet welded to a hollow hexagonal mandrel in the center, as seen in Figure 4.11. The shape of the mandrel was inferred by its cloudy appearance from the XCT Figure 4.12.

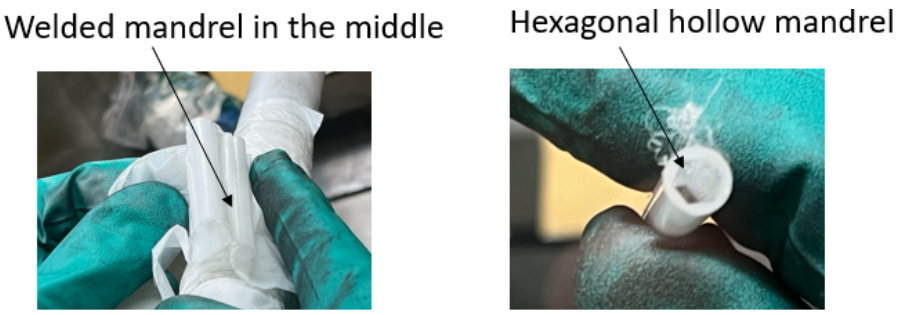

Figure 4.11: Welded hollow hexagonal plastic mandrel observed

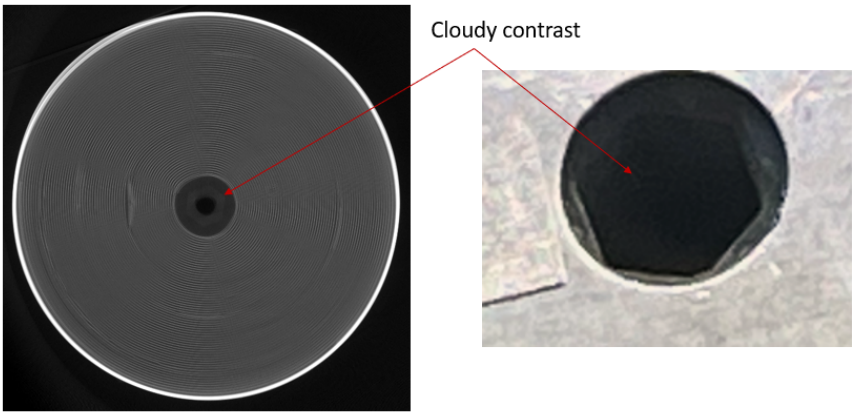

Figure 4.12: Hexagon shaped hollow mandrel

4.2.4 XCT Analysis and Correlation with Cell Teardown

This section presents the results of the XCT scan of the BYD 4680 cell, comparing the images to those obtained from cell teardown. Selected XCT images are included

to illustrate how various components within the cell can be identified solely from XCT imaging.

Figure 4.13 shows the complete XCT scan of the TO with clearly labeled components. In the image, bright spots indicate the presence of high-density metal (e.g. steel, copper, nickel etc.), while dull spots represent the presence of low-density metal (e.g. aluminium). The brightness of these spots is related to the density and X-ray attenuation properties of the materials. For example, steel is primarily composed of iron which has high density, thereby attenuating X-rays more strongly and appears brighter, whereas metal like aluminium, being less dense, have lower attenuation and thus appear relatively duller [39]. The bright areas confirm the presence of a high-density metal at the anode side of the cell. In contrast, the cathode side appears dimmer, highlighting the difference in material density and composition.

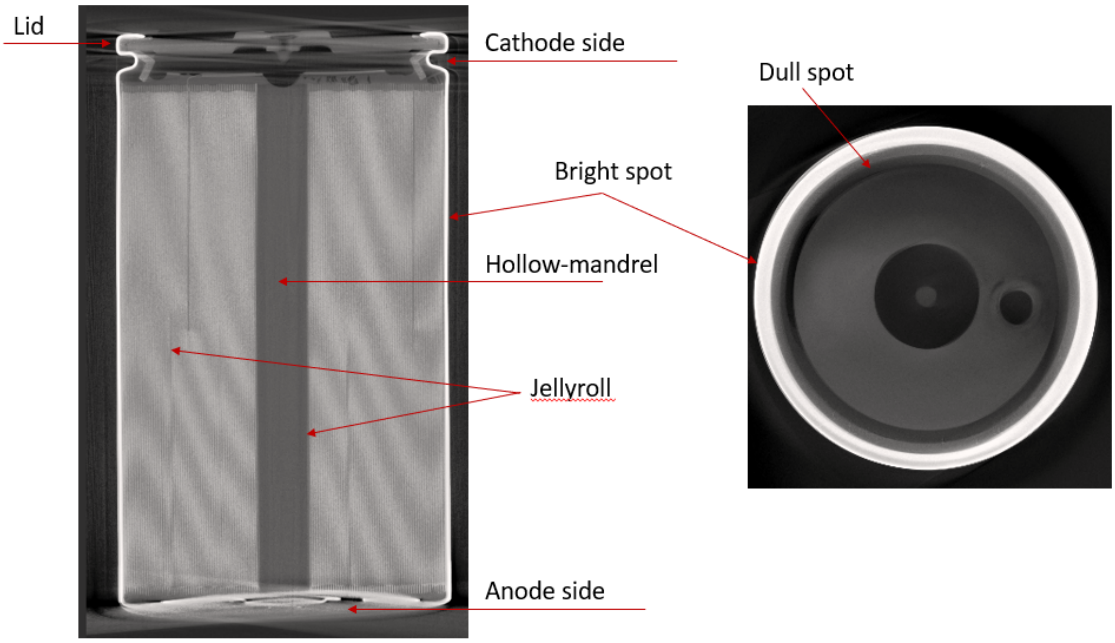

Figure 4.13: Full XCT picture of a BYD 4680 cell showing different components

Figure 4.14 illustrates the cell's safety vent, also visible in the corresponding XCT image. The vent, made of aluminium, is encapsulated by a plastic film. This distinction is evident due to the differences in contrast observed in the figure. The top layer is identified as plastic because of its pale grayscale, evident by a faint gray appearance, while the bottom layer is identified as aluminium due to its relatively moderate grayscale, evident by the thick solid gray appearance.

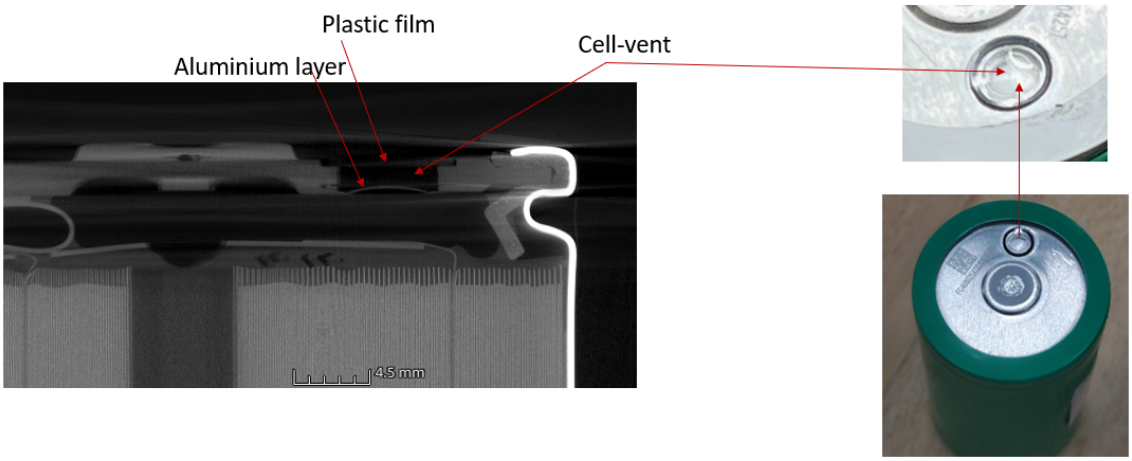

Figure 4.14: Safety vent for the cell

In this cell, the positive terminal is the cap, possibly made of aluminium [5], and the negative terminal is the cell body, made of steel-casing. After opening the positive terminal, an insulating blue plastic disc (Table 4.4) was observed to be placed below the cathode disc to prevent any short circuits between the electrodes.

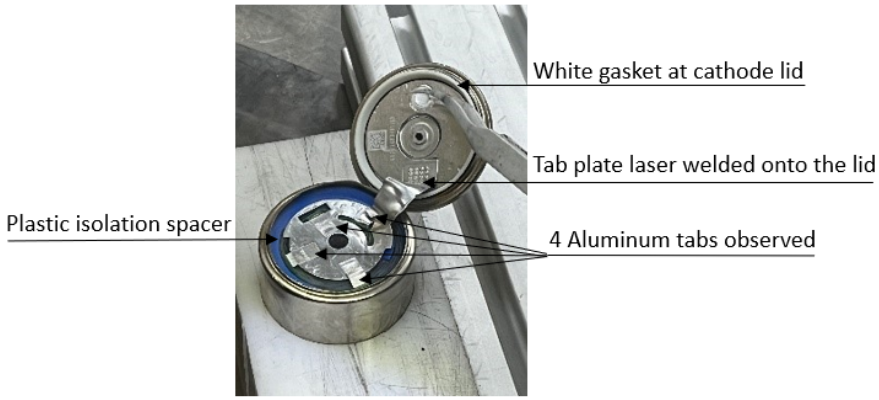

Figure 4.15: Exploded view from top depicting the isolation spacer, metal tabs and laser welds

Figure 4.16: The blue plastic isolating plate can be seen underneath the cathode disc

The cathode side tabs from the jellyroll are folded around and welded onto the cathode disc, which can be observed in the XCT image below being compared to its corresponding teardown image.

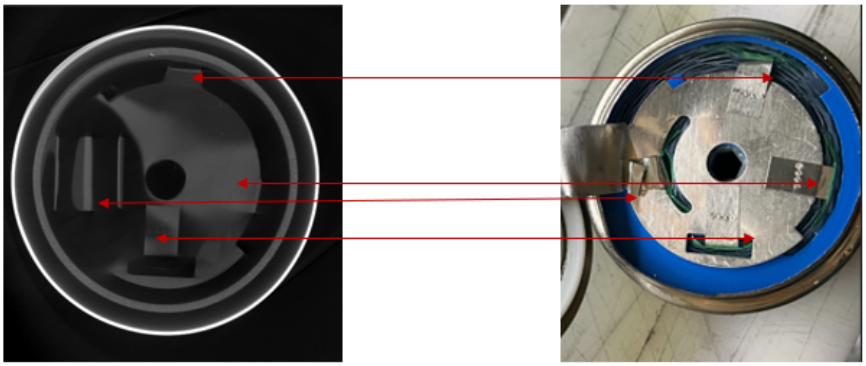

Figure 4.17: Four visible cathode side tabs can be observed (red arrows) in both pictures

Figures 4.18 and 4.19 depict the welding arrangement on the anode and cathode side, respectively. The negative terminal of the cell is laser welded to the anode disc, and laser welding is also used to attach the anode tabs to the anode disc. Figures 4.20 and 4.21 illustrate the XCT images of laser welding used to attach the cathode tabs to the cathode disc and the cathode disc to the positive terminal via an aluminium strip.

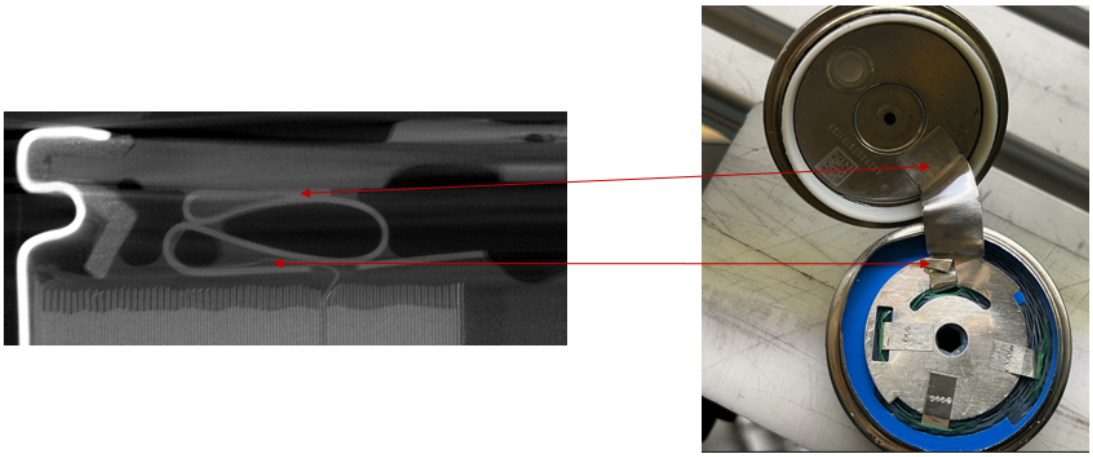

Figure 4.18: Welding arrangement between the cathode disc, positive terminal and cathode tab

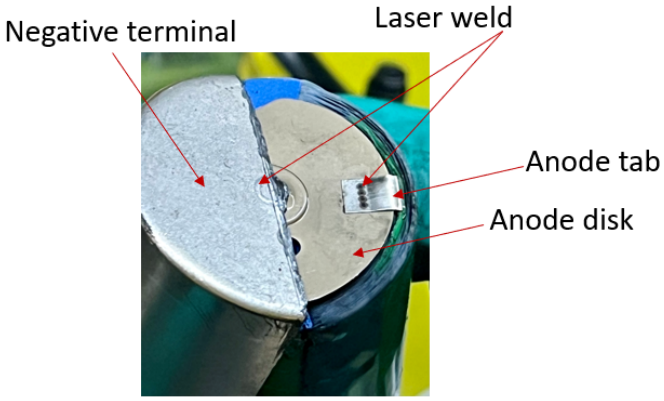

Figure 4.19: Welding arrangement between the negative terminal, anode disc and anode tab

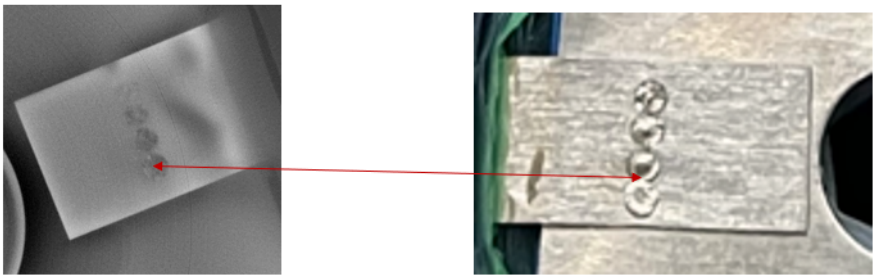

Figure 4.20: Cathode tab laser welded onto the cathode disc

Figure 4.21: Cathode disc laser welded onto the positive terminal

Figure 4.22 displays the XCT image that highlights the electrolyte filling hole, identified by a rivet-shaped plug that acts as a sealant. The red arrows indicate the plug observed during the teardown, positioned directly above the mandrel.

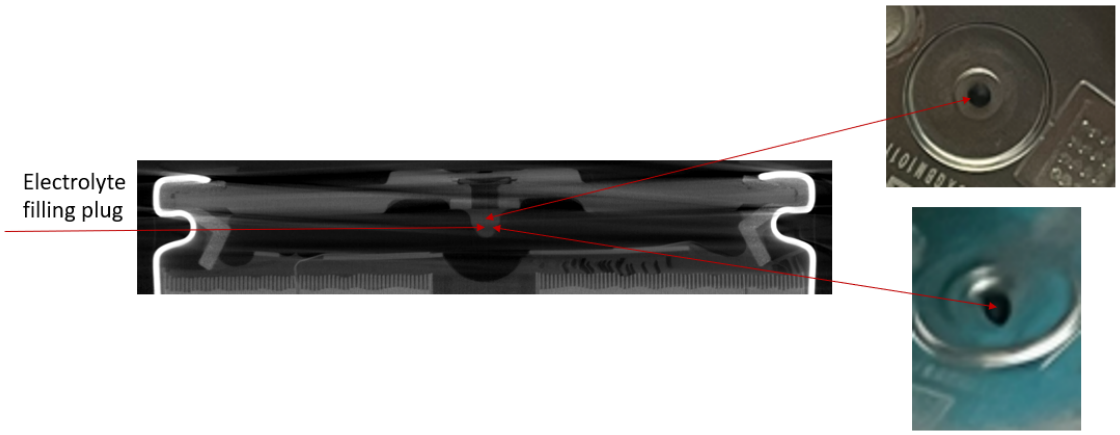

Figure 4.22: Electrolyte filling hole depicted

Figure 4.23 illustrates the various components of the cell as captured in the XCT image, highlighting the cathode, anode, separator and cell crimp. The separator is distinguished by the cloudy contrast portrayed in the figure, while air voids are visible within the heterogeneous mixture of the electrolyte. The presence of dark spots in the image indicates these voids, potentially caused by the clustering of separator sheets due to electrolyte wetting.

The cathode is observed by the thicker gray area, contrasting with the thinner and longer anode, as shown in Figure 4.23. The electrode alignment seems straight, with no signs of electrode bending even from where the cathode tab is drawn out.

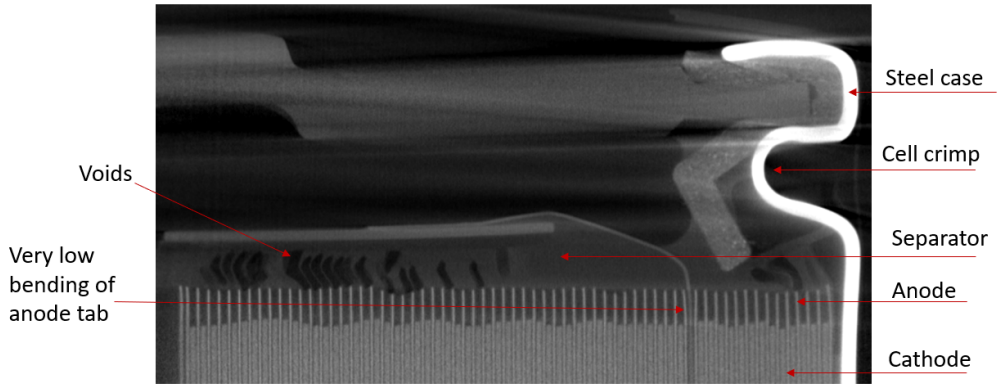

Figure 4.23: Different components of the cell as observed in XCT from cathode side

The dim regions in the XCT images represent the cathode tab, while the bright regions indicate the anode tab, as shown in Figure 4.24. This contrast is due to the difference in the atomic weights of the tab materials as explained in Section 2.2.1. The cathode and anode tabs are made of aluminium and nickel, respectively as seen with SEM-EDX analysis confirmed in Tables 4.1 and 4.2.

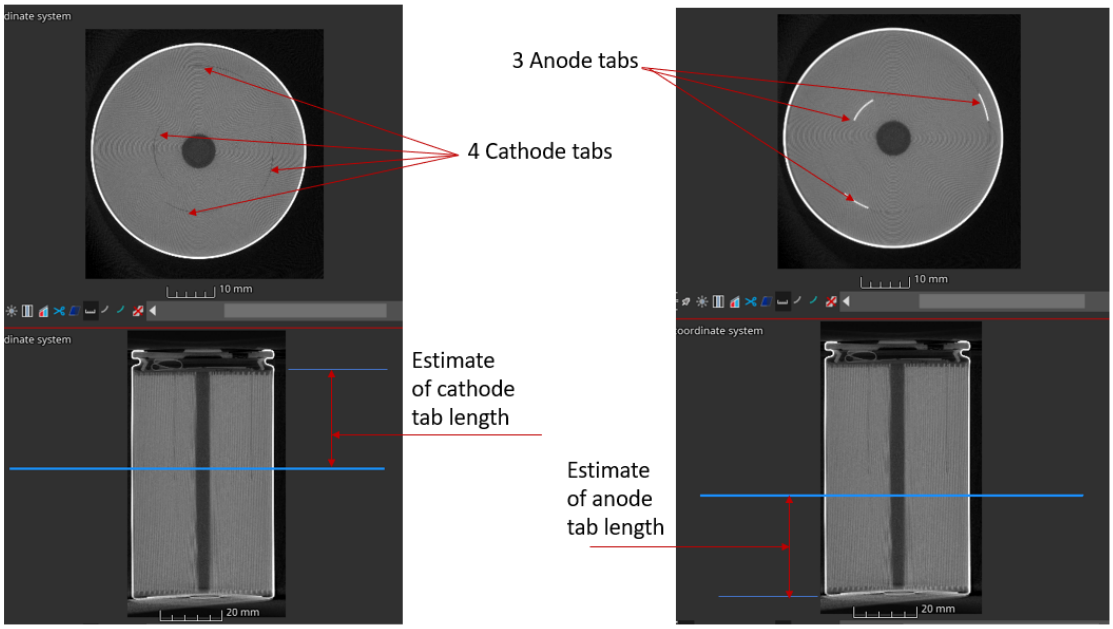

Figure 4.24: Electrode identification and their respective tab-length estimation

An approximate assessment of the tab lengths can also be made by examining the lower part of Figure 4.24. The blue horizontal line in the figure, when adjusted in the myVGL software, scans the cell along its length in a downward direction, revealing its internal components. As the blue line is pulled down, the cathode tabs begin to disappear and the anode tabs become visible, providing a rough estimate of the tab lengths at each electrode end.

In Figure 4.25, a comparison between the jellyrolls of BYD and Tesla 4680 cylindrical cells is presented. The Tesla cell features a tab-less design, in contrast to the tab design found in the BYD cell. Furthermore, the BYD jellyroll exhibits a tightly packed structure, while the Tesla jellyroll displays some excess space between its rolls. This disparity can be attributed to the utilization of relatively longer electrodes and separators in the BYD cell as summarized in Tables 4.1, 4.2 and 4.3. In comparison, the cathode and anode lengths of the Tesla cell were relatively shorter at 3.2 and 3.4 meters, respectively [5].

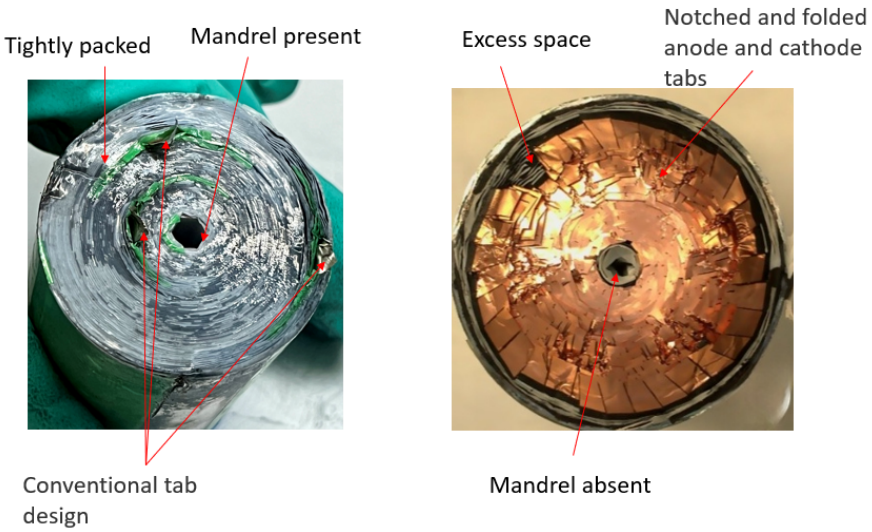

Figure 4.25: Left: BYD 4680 jellyroll; Right: Tesla 4680 jellyroll. Figure taken from [5]

Figure 4.26 illustrates the tab arrangements in four different cell types, including the BYD cell used thoughout this thesis work. The LG 18650 cell features a single tab at each electrode end, while the Sony 21700 cell is equipped with two tabs on the anode and cathode [1]. The Tesla 4680 cell utilizes a design that resembles multiple notches [5]. In contrast, the BYD 4680 cell has three tabs on the anode side and four tabs on the cathode side, as shown in Figure 4.24.

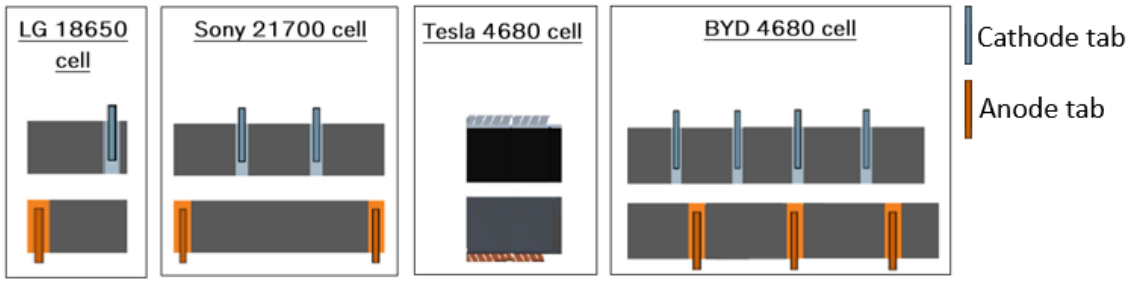

Figure 4.26: Arrangement of tabs on electrodes for different cells. Figure inspired from [1, 5]

4.3 Electrical Characterization

This section presents the results of electrical testing performed on the TO.

4.3.1 Reference Performance Test

4.3.1.1 Pulse Test

The DCIRs, obtained from a 10-second discharge pulse test, at 10%, 30%, 50%, 70% and 90% SOC for 21 cells are given in Table 4.5. Furthermore, those values are graphically represented in Figure 4.27 where the DCIR at 10% and 30% are higher than the resistances at higher SOC.

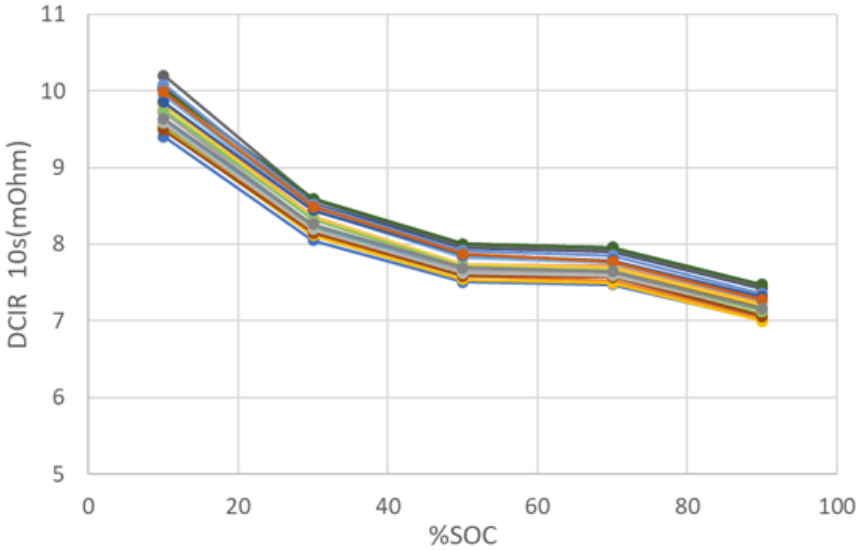

Figure 4.27: DCIR vs SOC

SoC (%)	DCIR (10s) (mΩ)
90	7.2 ± 0.1
70	7.7 ± 0.1
50	7.7 ± 0.2
30	8.3 ± 0.2
10	9.8 ± 0.2

Table 4.5: State of Charge (SOC) and corresponding DCIR values

4.3.1.2 Capacity Check

Figure 4.28 refers to the current and temperature profiles for a C/3 charge and discharge of the test object. The average discharge capacity value at C/3 over 25°C for 8 cells was found to be 15.6 ± 0.1 Ah.

It is observed that the positive pole exhibits a lower temperature trend compared to the negative pole. This difference might arise from the number of tabs and the materials used for the tabs at the cathode and anode. The cathode tabs are made of aluminium, which has a higher thermal conductivity than the nickel used for the negative tabs, allowing it to dissipate heat more efficiently. Furthermore, from Tables 4.1 and 4.2, there are four aluminium tabs and three nickel tabs. Therefore, the positive pole is seen to have a lower temperature than the negative pole. The negative pole shows higher temperatures than the cell-body center (T-Batt) likely due to the temperature build-up caused by the resistance of the current cables attached to the cell terminal. The cell temperature profile depends on the resistance at different SOCs and on the temperature build-up at the end of charge and discharge.

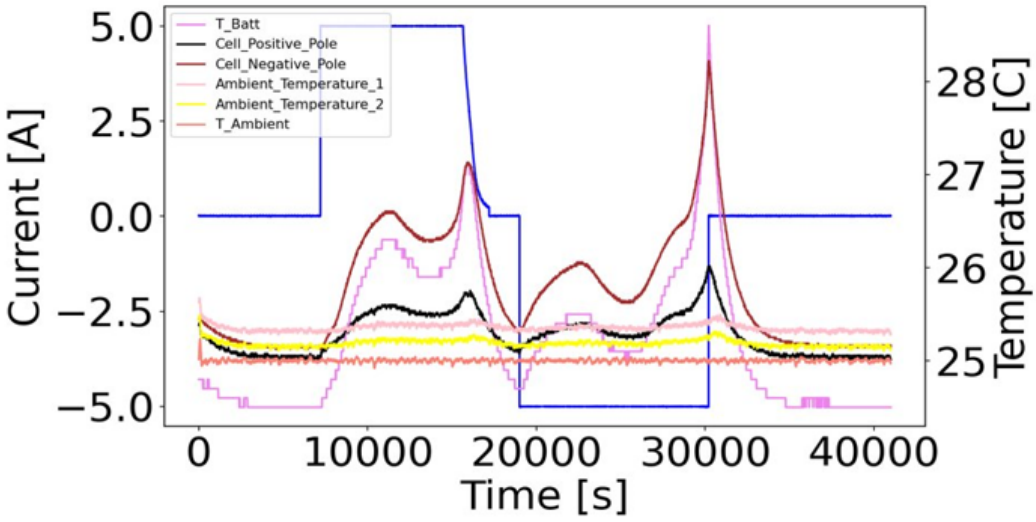

Figure 4.28: Current and temperature profile during CC-CV charge and CC discharge at C/3

4.3.1.3 Pseudo OCV Test

Figure 4.29 depicts the C/25 charge and discharge voltage profile of the cell, that remains nearly constant over a wide SOC range (roughly 20-60% and 70-90% SOC). This behavior makes it challenging to determine the SOC level solely based on the cell voltage. Furthermore, at high SOC levels, the resistance is lower (Figure 4.27), so the voltage does not drop as significantly during discharge as it does at SOC close to 0%.

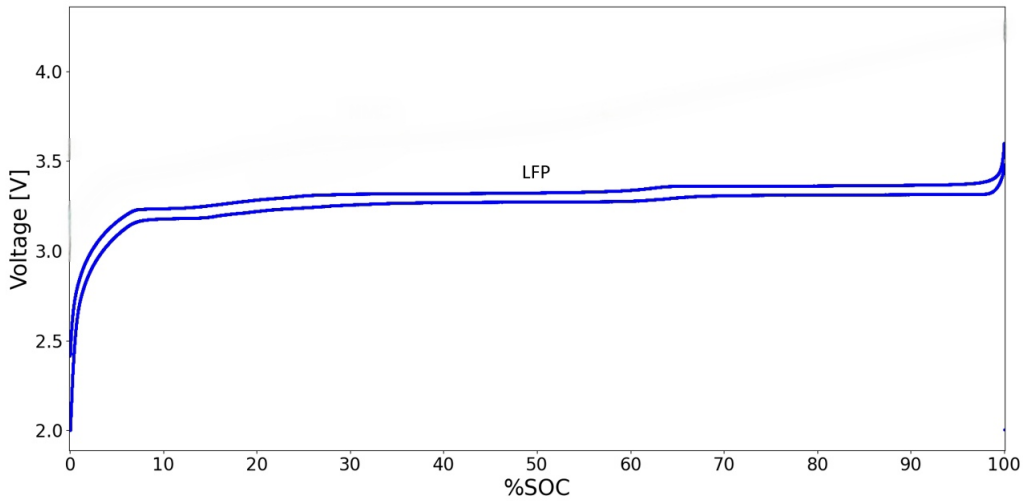

Figure 4.29: Voltage profile vs. SOC for C/25 charge and discharge sweeps

4.3.2 RCTs at -10°C and 25°C

In Figure 4.30 & 4.31, the discharge profiles at different C-rates are depicted, at initial temperatures of -10°C and 25°C respectively. At the former temperature, the

internal resistance is high, as can be seen from the very steep voltage decline, and causes the temperature of the cell to rise rapidly. As the cell discharges and its temperature rises, the cell resistance decreases, as can be seen in the voltage profile. Due to heat generation and lower resistance, the capacity registered at 1C is higher than at lower C-rates.

At 25°C (Figure 4.31), the initial voltage drop at higher SOC is less pronounced than in Figure 4.30. As the cell continues to discharge and the SOC decreases, the internal resistance increases, leading to a gradual rise in cell temperature, and for the cell temperature range shown, the capacity registered at 1C is as expected less than at lower C-rates.

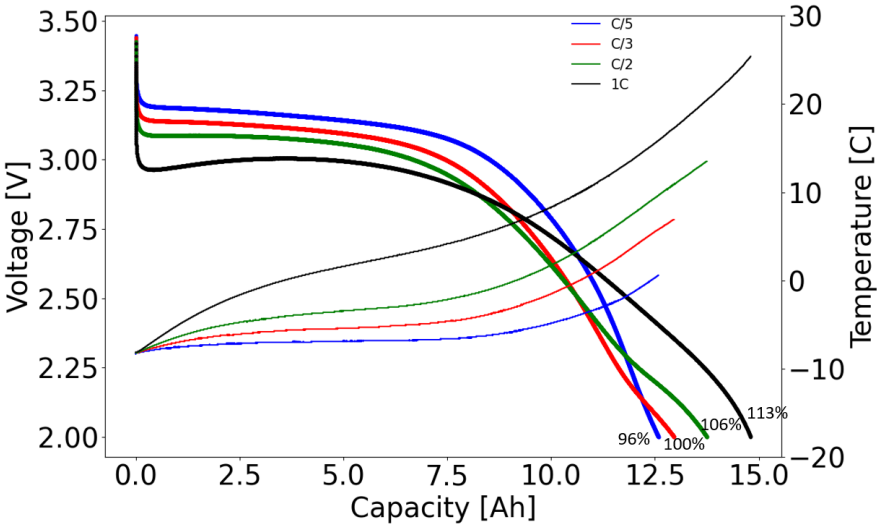

Figure 4.30: Voltage and temperature profiles of a cell discharged at different C-rates with an external temperature of -10°C

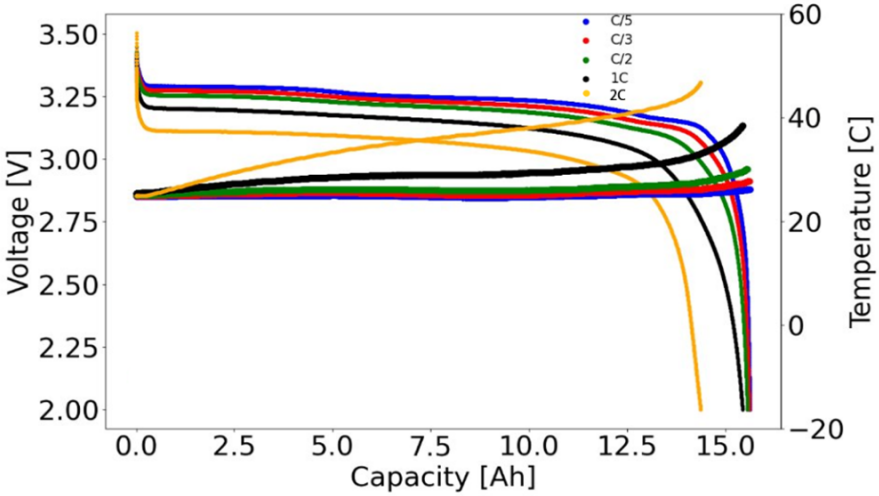

Figure 4.31: Voltage and temperature profiles of a cell discharged at different C-rates with an external temperature of 25°C

4.3.3 EIS

A simplified Randles circuit (Figure 4.32) was used to fit the EIS data and extract R_{ct} at different SOCs (10%, 30%, 50%, 70%, and 90%) during charge and discharge. The frequency region where diffusion took place (in the Nyquist plot usually represented by a straight line), was not considered to perform the data fitting. In the range 0-90% SOC, the resistance decreases with increasing SOCs, yet hysteresis is observed between the R_{cts} for the charge and discharge (Figure 4.32).

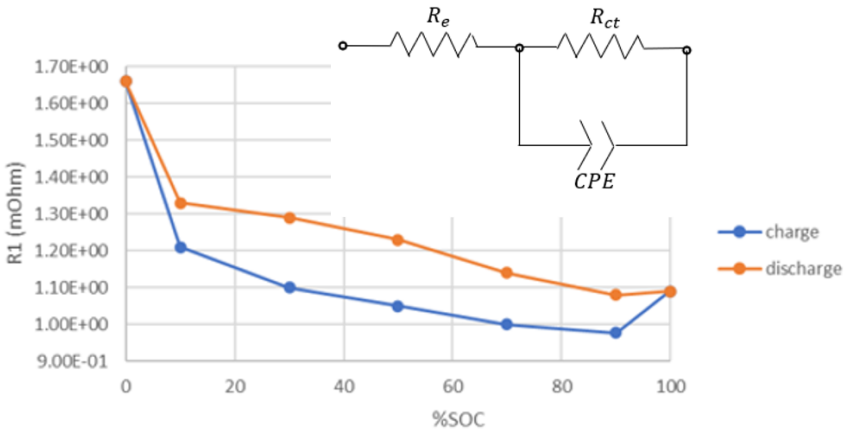

Figure 4.32: R_{ct} at different SOC when charging and discharging the cell

5
Conclusion and Future Outlook

In this section, the conclusion from the thesis and some future outlook are presented.

5.1 Conclusion

- A cylindrical BYD 4680 LFP cell was opened and its design was thoroughly studied.
- Two different cell-opening methodologies were explored, and an attempt was made to propose a novel approach capable of mitigating the cons of explored methodologies.
- The tab architecture of the BYD cell was found to be very different from the Tesla 4680 cell, showcasing 4 tabs on the cathode and 3 tabs on the anode side that resembled a conventional standard design rather than a tabless design.
- The BYD jellyroll appeared notably denser than the Tesla jellyroll, as illustrated in Figure 4.25. This discrepancy could be attributed to the significant difference in electrode lengths, with the BYD cell's electrodes extending approximately 2 meters longer than those of the Tesla.
- During cycling, the positive terminal temperature was lower than the negative side, likely due to the difference in material used for electrode tabs and their numbers.

5.2 Outlook

For future outlook, aging tests could be explored on this cell. Additionally, a tabless cylindrical cell could be opened using the methodology developed in this thesis, and the results from electrical testing could be used as a benchmark to conduct a comparative study between tabless and tab 46xx cylindrical cell architectures.

Bibliography

[1] S. Baazouzi, N. Feistel, J. Wanner, I. Landwehr, A. Fill, and K. P. Birke, "Design, properties, and manufacturing of cylindrical li-ion battery cells—a generic overview," *Batteries*, vol. 9, no. 6, p. 309, 2023.

[2] H. Pegel, D. Wycisk, and D. U. Sauer, "Influence of cell dimensions and housing material on the energy density and fast-charging performance of tabless cylindrical lithium-ion cells," *Energy Storage Materials*, vol. 60, p. 102796, 2023.

[3] R. Zhang and B. D. Ulery, "Synthetic vaccine characterization and design," *Journal of Bionanoscience*, vol. 12, no. 1, pp. 1–11, 2018.

[4] A. Rastegarpanah, J. Hathaway, M. Ahmeid, S. Lambert, A. Walton, and R. Stolkin, "A rapid neural network–based state of health estimation scheme for screening of end of life electric vehicle batteries," *Proceedings of the Institution of Mechanical Engineers, Part I: Journal of Systems and Control Engineering*, vol. 235, no. 3, pp. 330–346, 2021.

[5] M. Ank, A. Sommer, K. A. Gamra, J. Schöberl, M. Leeb, J. Schachtl, N. Streidel, S. Stock, M. Schreiber, P. Bilfinger, *et al.*, "Lithium-ion cells in automotive applications: Tesla 4680 cylindrical cell teardown and characterization," *Journal of The Electrochemical Society*, vol. 170, no. 12, p. 120536, 2023.

[6] J. B. Quinn, T. Waldmann, K. Richter, M. Kasper, and M. Wohlfahrt-Mehrens, "Energy density of cylindrical li-ion cells: a comparison of commercial 18650 to the 21700 cells," *Journal of The Electrochemical Society*, vol. 165, no. 14, pp. A3284–A3291, 2018.

[7] A. Frank, J. Sturm, M. Steinhardt, A. Rheinfeld, and A. Jossen, "Impact of current collector design and cooling topology on fast charging of cylindrical lithium-ion batteries," *ECS Advances*, vol. 1, no. 4, p. 040502, 2022.

[8] T. G. Tranter, R. Timms, P. R. Shearing, and D. Brett, "Communication—prediction of thermal issues for larger format 4680 cylindrical cells and their mitigation with enhanced current collection," *Journal of The Electrochemical Society*, vol. 167, no. 16, p. 160544, 2020.

[9] B. Group *et al.*, "Mehr leistung, co2-reduzierte produktion, kosten deutlich reduziert: Die bmw group setzt in der neuen klasse ab 2025 innovative bmw batteriezellen im rundformat ein. 2022."

[10] "Sustainable development goals," *United Nations*, 2024. [Online]. Available: `https://sdgs.un.org/goals` [Accessed: April 2024].

[11] "Sustainable development goals," *United Nations*, 2024. [Online]. Available: `https://sdgs.un.org/goals/goal7` [Accessed: April 2024].

[12] "Sustainable development goals," *United Nations*, 2024. [Online]. Available: `https://sdgs.un.org/goals/goal9` [Accessed: April 2024].

[13] "Sustainable development goals," *United Nations*, 2024. [Online]. Available: https://sdgs.un.org/goals/goal13 [Accessed: April 2024].

[14] "Sustainable development goals," *United Nations*, 2024. [Online]. Available: https://sdgs.un.org/goals/goal12 [Accessed: April 2024].

[15] "What is a battery?," *University of Washington*, 2024. [Online]. Available: https://depts.washington.edu/matseed/batteries/MSE/battery.html [Accessed: March 2024].

[16] E. R. Cohen, *Quantities, units and symbols in physical chemistry*. Royal Society of Chemistry, 2007.

[17] H. Berg, *Batteries for electric vehicles: materials and electrochemistry*. Cambridge university press, 2015.

[18] K. P. Logakannan, F. Zhu, D. Sypeck, J. Deng, and S. Kim, "Impact response of prismatic li-ion battery jellyrolls and cells," *International Journal of Impact Engineering*, vol. 170, p. 104352, 2022.

[19] H. H. Heimes, A. Kampker, C. Lienemann, M. Locke, C. Offermanns, S. Michaelis, and E. Rahimzei, *Lithium-ion battery cell production process*. PEM der RWTH Aachen University, 2018.

[20] D. P. Finegan, E. Darcy, M. Keyser, B. Tjaden, T. M. Heenan, R. Jervis, J. J. Bailey, N. T. Vo, O. V. Magdysyuk, M. Drakopoulos, *et al.*, "Identifying the cause of rupture of li-ion batteries during thermal runaway," *Advanced Science*, vol. 5, no. 1, p. 1700369, 2018.

[21] A. Ran, S. Chen, S. Zhang, S. Liu, Z. Zhou, P. Nie, K. Qian, L. Fang, S.-X. Zhao, B. Li, *et al.*, "A gradient screening approach for retired lithium-ion batteries based on x-ray computed tomography images," *RSC advances*, vol. 10, no. 32, pp. 19117–19123, 2020.

[22] A. Mohammed and A. Abdullah, "Scanning electron microscopy (sem): A review," in *Proceedings of the 2018 International Conference on Hydraulics and Pneumatics—HERVEX, Băile Govora, Romania*, vol. 2018, pp. 7–9, 2018.

[23] "Principles of scanning electron microscopy," *Thermo Fisher Scientific*, 2024. [Online]. Available: https://www.thermofisher.com/se/en/home/materials-science/learning-center/applications/scanning-electron-microscope-sem-electron-column.html [Accessed: March 2024].

[24] M. Scimeca, S. Bischetti, H. K. Lamsira, R. Bonfiglio, and E. Bonanno, "Energy dispersive x-ray (edx) microanalysis: A powerful tool in biomedical research and diagnosis," *European journal of histochemistry: EJH*, vol. 62, no. 1, 2018.

[25] D. Andre, M. Meiler, K. Steiner, C. Wimmer, T. Soczka-Guth, and D. Sauer, "Characterization of high-power lithium-ion batteries by electrochemical impedance spectroscopy. i. experimental investigation," *Journal of Power Sources*, vol. 196, no. 12, pp. 5334–5341, 2011.

[26] P. Iurilli, C. Brivio, and V. Wood, "On the use of electrochemical impedance spectroscopy to characterize and model the aging phenomena of lithium-ion batteries: a critical review," *Journal of Power Sources*, vol. 505, p. 229860, 2021.

[27] J. Vetter, P. Novák, M. R. Wagner, C. Veit, K.-C. Möller, J. Besenhard, M. Winter, M. Wohlfahrt-Mehrens, C. Vogler, and A. Hammouche, "Ageing

mechanisms in lithium-ion batteries," *Journal of power sources*, vol. 147, no. 1-2, pp. 269–281, 2005.

[28] J. J. Giner-Sanz, E. Ortega, and V. Pérez-Herranz, "Application of a montecarlo based quantitative kramers-kronig test for linearity assessment of eis measurements," *Electrochimica Acta*, vol. 209, pp. 254–268, 2016.

[29] A. Lasia, "Electrochemical impedance spectroscopy and its applications," in *Modern aspects of electrochemistry*, pp. 143–248, Springer, 2002.

[30] D. Andre, M. Meiler, K. Steiner, H. Walz, T. Soczka-Guth, and D. Sauer, "Characterization of high-power lithium-ion batteries by electrochemical impedance spectroscopy. ii: Modelling," *Journal of Power Sources*, vol. 196, no. 12, pp. 5349–5356, 2011.

[31] M. Bruch, L. Millet, J. Kowal, and M. Vetter, "Novel method for the parameterization of a reliable equivalent circuit model for the precise simulation of a battery cell's electric behavior," *Journal of Power Sources*, vol. 490, p. 229513, 2021.

[32] C.-M. Park, S. Yoon, S.-I. Lee, J.-H. Kim, J.-H. Jung, and H.-J. Sohn, "Erratum: High-rate capability and enhanced cyclability of antimony-based composites for lithium rechargeable batteries (j. electrochem. soc., 154, a917 (2007))," *Journal of The Electrochemical Society*, vol. 154, no. 11, p. S19, 2007.

[33] J. Holloway, F. Maddar, M. Lain, M. Loveridge, M. Copley, E. Kendrick, and D. Greenwood, "Determining the limits and effects of high-rate cycling on lithium iron phosphate cylindrical cells," *Batteries*, vol. 6, no. 4, p. 57, 2020.

[34] "Gs mega line," *Labex*, 2024. [Online]. Available: `https://labex.com/wp-content/uploads/GS_MEGA_Line_broschyr.pdf` [Accessed: March 2024].

[35] "Citovac with built-in vacuum ejector," *Struers*, 2024. [Online]. Available: `https://publications.struers.com/brochures/english/citovac/?page=1` [Accessed: March 2024].

[36] "Why 4-point measurements?," *BioLogic*, 2024. [Online]. Available: `https://www.biologic.net/topics/why-4-points-measurements/` [Accessed: May 2024].

[37] M. D. Murbach, B. Gerwe, N. Dawson-Elli, and L.-k. Tsui, "impedance. py: A python package for electrochemical impedance analysis," *Journal of Open Source Software*, vol. 5, no. 52, p. 2349, 2020.

[38] J. Ni, H. Zhou, J. Chen, and X. Zhang, "Lifepo4 doped with ions prepared by co-precipitation method," *Materials letters*, vol. 59, no. 18, pp. 2361–2365, 2005.

[39] A. Naji, M. Jaafar, E. Ali, and S. Al-Ani, "X-ray attenuation and reduction of backscattered radiation," *Applied Physics Research*, vol. 8, no. 4, pp. 92–102, 2016.

DEPARTMENT OF INDUSTRIAL AND MATERIALS SCIENCE
CHALMERS UNIVERSITY OF TECHNOLOGY
Gothenburg, Sweden
www.chalmers.se

CHALMERS
UNIVERSITY OF TECHNOLOGY